Phonon-Mediated Temperature Dependence of Er^{3+} Optical Transitions in Single-Crystal Er_2O_3

By

Adam Dee Dodson

Dissertation

Submitted to the Faculty of the

Graduate School of Vanderbilt University

in partial fulfillment of the requirements

for the degree of

DOCTOR OF PHILOSOPHY

in

Physics

May 10, 2024

Nashville, Tennessee

Approved:

Norman H. Tolk, Ph.D.

Jimmy L. Davidson, Ph.D.

Sokrates T. Pantelides, Ph.D.

Sait A. Umar, Ph.D.

Thomas W. Kephart, Ph.D.

ACKNOWLEDGMENTS

I would like to thank my advisor Norman Tolk for his mentorship and unwavering optimism. I thank my PhD committee members; Dr. Jimmy Davidson, Dr. Sokrates Pantelides, Dr. Sait Umar and Dr. Thomas Kephart for their guidance and support. I would like to give a special thanks to Dr. Leornard Feldman and Dr. Anthony Hmelo for their guidance and support. I would also like to thank group memebers past and present; Dr. Andrey Baydin, Dr. Halina Krzyzanowska, Dr. Andrew O'Hara, Hongrui Wu as well as Dr. Benjamin Lawrie and many others that have contributed to the success and enjoyment of my research. I also thank my parents for all of their encouragement and guidance over the years. More than anything I thank my wonderful wife Amanda and son David for making this process both pleasant and possible. I could not have done it without you.

TABLE OF CONTENTS

Page

LIST OF TABLES

LIST OF FIGURES

CHAPTER 1

Introduction

1.1 Motivation

Rare-earth elements have found applications in light phosphors [4; 5], lasers, optical thermometry [6; 7; 8], telecom amplifiers [7; 9], and emerging applications in quantum information science [10; 11]. Rare earth ions dopants have attracted growing interest because of their intrinsic spin-phonon interfaces, atomic-like character embedded in solid-state systems and and compatibility with solid-state integration methods. This is a direct result of the fact that the 4f-4f electronic transitions in rare-earth ions are shielded from their local environment by the filled orbitals of 5s and 5p with are further from the nucleus than the 4f shells. One of the rare-earth elements, erbium (Er), exhibits compelling properties because of the luminescence in the telecom band which originates from the $^4I_{13/2} \rightarrow {}^4I_{15/2}$ which emits around 1.5-microns, the absorption minima of optical fibers. As a result, this transition, and by extension Er, may play a role in practical and scalable quantum networks[12; 13].

One of the main challenges that rare earth ions present in QIS is the intrinsically low radiative emission rate of the 4f-4f intrashell transitions. These emission rates can be improved by coupling ions into nanophotonic cavities, which has lead to Purcell enhancement of several orders of magnitude. One downside of this is that desired properties, such as optical and spin coherence, are often negatively impacted due to nearby interfaces and material defects. Additionally, well-controlled incorporation methods used in device creation like ion implantation can leave residual defects which modify the desired properties of rare-earth emitters. However, it is notable that not all impacts from interfaces and defects are necessarily detrimental. Recent works have suggested the possibility of utilizing the defect-induced inhomogeneous broadening of rare earth optical transitions for dense

spectral multiplexing of qubits or memories. For these reasions, important to understand the influence of local perturbations, including nearby interfaces and defects on the desired photophysical properties of rare earth ions. It is the aim of this thesis to to establish a baseline of behavior for the photoluminesence properties of Er^{3+} in Er_2O_3 in preparation for studies on the influence of local perturbations on the photophysical properties of Er^{3+}.

The theory of rare-earth optical emission in solids, called Judd-Ofelt theory, was developed in the 1960's [14; 15; 16; 17]. This theory states that symmetry breaking from the crystal field of the host material gives rise to closely spaced Stark-split level with mixed parity, between which electric dipole transitions can occur. Despite the perturbation from the crystal field, the electrons in the 4f shell are partially shielded by filled outer shell electrons and the transitions within the 4f shell retain atomic-like character with a relatively weak dependence upon the host material.

It is well established that the 4f electrons couple weakly to the phonons of the host material [18; 19]. Despite this, the long radiative lifetime of these transitions permits robust non-radiative processes. This has permitted many studies utilizing temperature dependent photoluminescence to characterize the interactions of Er^{3+} with its local environment [9; 20; 21; 22; 23; 24; 25; 26; 27; 28; 29; 30; 31; 32; 33; 34; 35]. Following the analytical approach described by Auzel [18; 19], these studies have focused on using temperature dependent photoluminescence to characterize the interactions of Er^{3+} with its local environment, including phonon-assisted processes such as Stokes/anti-Stokes excitation, de-excitation of Er^{3+} ions, thermalization of closely spaced levels, and non-resonant energy transfer between rare-earth ions.

Despite their success, existing modeling approaches suffer from several limitations. First, modeling of the temperature dependence of photoluminescence grouped the Stark levels according to their respective $^{2S+1}L_j$ state and treated those groupings as single units rather than the individual Stark levels. This grouping prevented incorporating multiple Stokes and anti-Stokes excitations from the ground state. Second, the existing modeling

approach usually invoked an effective phonon energy associated with any excitation process rather than a phonon energy found in the host material. These limitations prevented existing models from providing an accurate description of the observations discussed in this thesis. It is clear that an improved model of the electron-phonon interactions is required.

1.2 Statement of Work

In this thesis, the electron-phonon interactions of Er^{3+} with its host lattice Er_2O_3 are studied using temperature dependent photoluminescence. We report new measurements of the temperature dependent photoluminescence of the ${}^4S_{3/2} \rightarrow {}^4I_{15/2}$, ${}^4S_{3/2} \rightarrow {}^4I_{13/2}$ and ${}^2H_{11/2} \rightarrow {}^4I_{15/2}$ transition manifolds of Er^{3+} in Er_2O_3. We also report a newly developed modeling approach that advances the existing modeling approach by making the following considerations. First, the individual Stark-split levels are considered rather than grouping them by their ${}^{2S+1}L_j$ level. Second, multiple Stokes and anti-Stokes excitations are permitted between the ground state and excited state rather than a single Stokes or anti-Stokes excitation between the ${}^{2S+1}L_j$ levels. Third, the phonon energies specific to Er_2O_3 are explicitly incorporated into the model rather than an effective phonon energy that is extracted by fitting the experimental data. This approach, which can be generalized to other rare earth ion systems, provides an accurate description of our data over the measured temperature range.

Our modeling effort also gives rise to two important conclusions. First, the electron-phonon coupling differs between ${}^{2S+1}L_j$ states. Second, the model predicts that the low temperature photoluminescent behavior of Er^{3+} varies significantly with small changes ($\sim$0.1 nm) in excitation wavelength. Both conclusions have important implications for any potential application.

1.3 Thesis Outline

This thesis is structured as follows:

Chapter 2 starts with a discussion of Er^{3+} in Er_2O_3, specifically how multiple perturba-

tions give rise to the electronic states relevant to this thesis. The perturbations are discussed in turn and the relevant Stark-split states are identified. The Laporte rule is discussed along with how the perturbation due to the crystal field of Er_2O_3 permits electric dipole transitions consistent with Judd-Ofelt theory.

Chapter 3 presents the temperature dependent photoluminescence measurements of the $^4S_{3/2} \rightarrow {}^4I_{15/2}$, $^4S_{3/2} \rightarrow {}^4I_{13/2}$ and $^2H_{11/2} \rightarrow {}^4I_{15/2}$ transition manifolds under 532 nm excitation. An analysis of this data is given which demonstrates that the temperature dependent photoluminescence of a given Stark-Stark transition depends only on the temperature dependence of the population fraction of the decaying Stark level.

Chapter 4 develops a theoretical model to predict the temperature dependence of the excited state population fractions. In this chapter, we extend existing theory of temperature dependence photoluminescence of rare earth ions and develop the machinery to allow consideration of the Stark-split levels of the ion, multiple Stokes and anti-Stokes excitations and incorporation of material-specific phonons. The result is a model capable of describing temperature dependent photoluminescence of these transitions in Er^{3+} in Er_2O_3 from 4 K to 300 K. The approach we take can be generalized and extended to other rare-earth ion systems.

Chapter 5 applies the theoretical model developed in Chapter 4 to our observations which were presented in Chapter 3. The influence of each model parameter on the output is discussed as well as the implications of the fit values. The chapter concludes with a brief discussion of a notable prediction of the model. Namely that the low temperature photoluminescence behavior of Er^{3+} varies significantly with small shifts in excitation wavelength ($\sim$0.1 nm).

Chapter 6 summaries the thesis and lists future directions and experiments that are an extension of the work discussed in this thesis.

CHAPTER 2

Er^{3+} in Er_2O_3

2.1 States of Er^{3+}

Identifying the relevant states of Er^{3+} described in this thesis requires an understanding of the electronic structure of Er $^{3+}$. We take the approach shown pictorially in Figure 2.1 and given in [16] for Eu^{3+}; begin with the central field Hamiltonian, H_0, due to the nucleus of the atom and add each perturbation in the order of magnitude for rare-earth ions. We will begin with the Aufbau principle which addresses the orbital filling order due to the central field [36; 37; 38]. Hund's 3 rules, which address electron-electron repulsion and spin-orbit coupling, will follow [37; 38; 39]. Finally, we will discuss the effect of the crystal field which splits the free ion levels and permits the transitions discussed in Chapter 3.

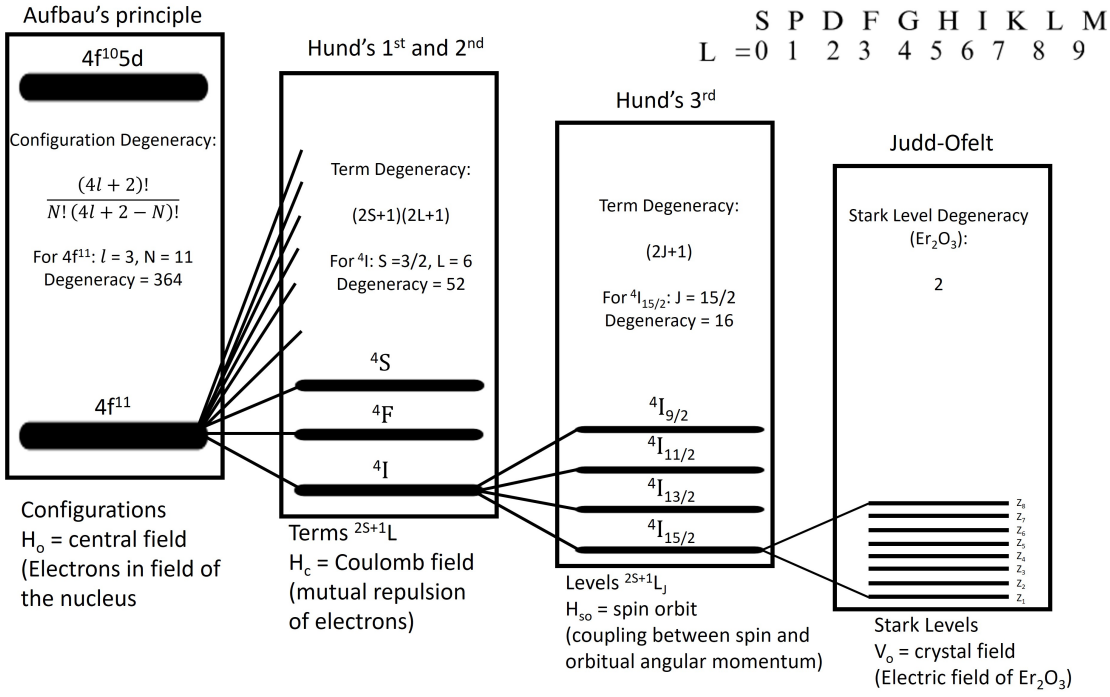

Figure 2.1: Progression of level splitting of Er^{3+} due to perturbations to the central field Hamiltonian. Note that the splittings are not uniform. It is shown this way for simplicity.

The Aufbau principle gives the filling order of the electronic shells in the ground state

configuration [36; 37; 38]. Electrons fill the lowest energy subshells first. Applied to Er^{3+} gives the electronic configuration is [Xe]$4f^{11}$, where [Xe] signifies that the core electrons of Er^{3+} have the same configuration as xenon. This principle considers only the central field of the nucleus in the Hamiltonian.

Hund's 3 rules are required to further specify the ground state of a multi-electron atom [37; 38; 39]. This is because of the electrostatic repulsion between electrons (Hund's 1st and 2nd rules) and spin-orbit coupling (Hund's 3rd rule). Beginning with Hund's 1st rule, also called Hund's rule of maximum multiplicity, which states that electrons are placed in orbitals to give the maximum total spin possible [37; 38; 39]. The spin multiplicity is given by 2S+1, where S is the total spin angular momentum for all electrons.

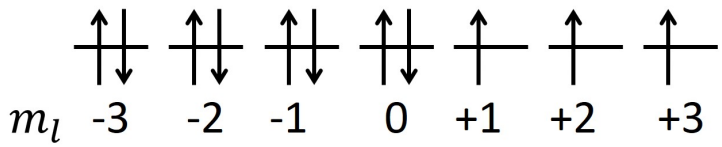

Figure 2.2: Filling of 4f shell based on Hund's 1st and 2nd rule. The magnetic quantum levels are denoted by m_l

Hund's 2nd rules states that if there are multiple terms with the same maximum spin multiplicity, the term with the largest total angular momentum, L, is the ground state [37; 38; 39].

The states that result from applying these two rules are given a term symbol: $^{2S+1}$L. The result of applying these rules is ^{4}I and is shown in Figure 2.2.

Hund's 3rd rule states that when subshells are half, the state with the lowest J has the lowest energy [37; 38]. If the subshell is more than half filled, the state with the highest J has the lowest energy. The value J is the total angular momentum quantum number. This value ranges between $|L-S|$ and $|L+S|$ in steps of 1.

That resultant state is labeled by a level symbol $^{2S+1}L_j$. From Figure 2.2, the shell is more than half filled. Given that S = 3/2 and L = 6, the lowest energy state has J=15/2 and the ground state of the free ion Er^{3+} is $^4I_{15/2}$. It is important to note that the perturbations

noted in Figure 2.1 mix the states together, such that the ground state is not purely $^4I_{15/2}$. Rather, in the free ion Er^{3+} the level is $0.985|^4I_{15/2}\rangle + 0.173|^2K_{15/2}\rangle$ [3]. Similar expansions can be found for the levels shown in Figure 2.3 [40]. Note that these expansions are altered slightly when Er^{3+} is incorporated into a material, due to the crystal field. Regardless, the traditional labeling scheme for the levels of multi-electron atoms omits all but the leading term, except in the case of nearly identical contribution, then the 2 leadings terms are sometimes noted (e.g. the $^2H_{11/2}$ state is sometimes reported as $(^2H,^4G)_{11/2}$). We will follow that tradition in this thesis. The free-ion Er^{3+} level diagram for the lowest 7 levels is given in Figure 2.3. The relevant levels for this thesis are $^2H_{11/2}$, $^4S_{3/2}$, $^4I_{13/2}$ and $^4I_{15/2}$.

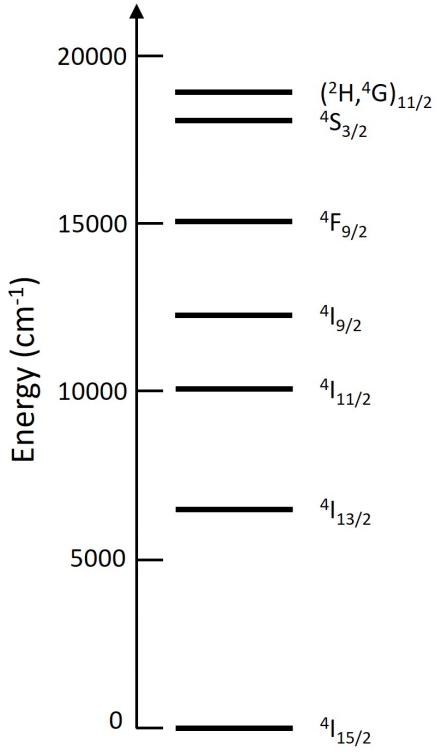

Figure 2.3: Lowest 7 levels of Er^{3+} [3]

The final perturbation noted in Figure 2.1 is the crystal field of Er_2O_3. For Er^{3+} ions at the sites with C_2 symmetry, each level shown in Figure 2.3 is further split into j+1/2 Stark levels. These levels retain a degeneracy of 2 because there is half-integer total spin and by Kramer's theorem [41] the degeneracy must be 2. The energies of these levels have

been well-studied by Gruber et. al. [1; 42] and we note the energies of the relevant levels in Table 2.1 using the labeling scheme originated by Gruber et. al. [1] The relevant Stark-split levels for this thesis are shown in Figure 2.4.

Stark-split Level	Energy (cm^{-1})	$^{2S+1}L_j$ Level
Z_1	0	$^4I_{15/2}$
Z_2	38	
Z_3	75	
Z_4	88	
Z_5	159	
Z_6	265	
Z_7	490	
Z_8	505	
Y_1	6510	$^4I_{13/2}$
Y_2	6542	
Y_3	6588	
Y_4	6594	
Y_5	6684	
Y_6	6840	
Y_7	6867	
E_1	18222	$^4S_{3/2}$
E_2	18308	
F_1	19033	$(^2H,^4G)_{11/2}$
F_2	19040	
F_3	19067	
F_4	19182	
F_5	19213	
F_6	19235	

Table 2.1: Stark-split energy levels of Er^{3+} in Er_2O_3. The levels are identified by the notation introduced by Gruber et. al. [1]

2.2 The Laporte Selection Rule and Judd-Ofelt Theory

The Laporte selection rule states that for electric dipole radiation, transitions between states of the same symmetry with respect to inversion are forbidden [43]. Functionally, this means that electric dipole transitions cannot occur between levels if the wavefunctions of those retain well-defined symmetry and their symmetry is identical. For the case of the free

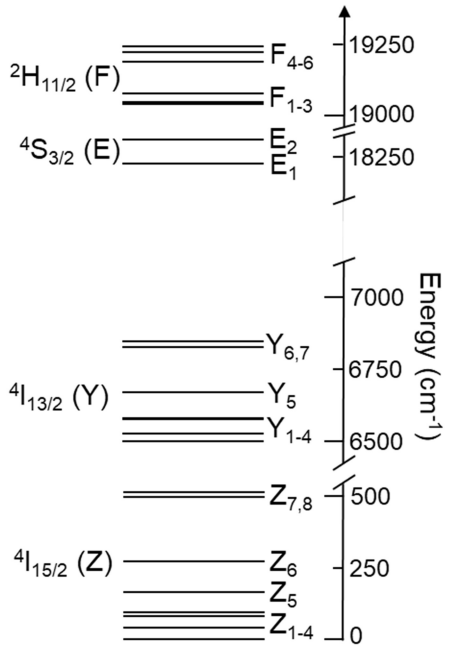

Figure 2.4: Stark-split levels of $^2H_{11/2}$, $^4S_{3/2}$, $^4I_{13/2}$ and $^4I_{15/2}$. Labeled according to Gruber et. al. [1] Note that $^2H_{11/2}$ is often labeled as $(^2H,^4G)_{11/2}$. The ^4G is dropped for convenience in labeling.

Er^{3+} ion, all of the states in Figure 2.3 possess odd symmetry [3] and there are no electric dipole allowed transitions between levels. The observations that such transitions occurred for rare-earth ions incorporated into solids lead to the development of Judd-Ofelt theory.

In the 1930's that emission spectra of rare earths presented a puzzle. In 1937, an article entitled "The Puzzle of Rare-Earth Spectra in Solids," [44] noted that the rare earths had sharp spectral lines consistent with transitions occurring between levels inside the 4f electronic shell. However, as noted above, these transitions are forbidden by the Laporte selection rule. It was not until the early 1960s that this was resolved in papers published by Judd [14] and Ofelt [15]. They showed that when a rare earth ion is incorporated into a solid host material, the rare earth ion can become optically active as a result of symmetry breaking of the host crystal field.

From perturbation theory, it is known that in the presence of a perturbation [45], to first order the perturbed wavefunctions, $|\Psi_n\rangle$, can be written as:

$$|\Psi_n\rangle = |\psi_n\rangle + \sum_m \frac{\langle\psi_m|V|\psi_n\rangle}{E_n - E_m}|\psi_n\rangle, \tag{2.1}$$

where $|\psi_n\rangle$ and $|\psi_m\rangle$ are the wavefunctions of the unperturbed states, E_n and E_m are the enegies of those states and V is the perturbation, which in this case is the crystal field. According to Judd-Ofelt theory, the odd-order parts of the crystal field when expanded as a series of spherical harmonics result in mixed parity states [16]. In the case of rare-earth ions, the states of opposite parity that are mixed in originate from shells above 4f, such as the 5d shell. Electric dipole transitions are allowed between these mixed parity states and this is seen experimentally as transitions between the Stark-split levels.

It is convenient to discuss this in terms of the point symmetry of the site occupied by the rare earth ion [16]. There are thirty-two crystallographic point groups. Those groups that have inversion as a symmetry element have no non-zero odd-order parts in the expansion of the crystal field (e.g. C_{3i}). Therefore, the resultant states retain definite parity and electric dipole transitions remain forbidden. It is those sites with a non-centrosymmetric crystal field, or in other words sites lacking inversion symmetry, that give rise to mixed parity states which allow electric dipole transitions (e.g. C_2). For the present thesis, it is sufficient to be aware of the mechanism that allows for the transitions. This is because, as will be demonstrated experimentally and discussed in Chapters 3 and 4, there is only a weak temperature dependence for the transition probabilities calculated using Judd-Ofelt theory between the states considered in this thesis. For a more complete treatment of Judd-Ofelt theory see [16; 17].

2.3 Single Crystal Er_2O_3

Erbium oxide is a rare earth sesquioxide which means it has a chemical composition of Er_2O_3 [9]. The most common polytype of Er_2O_3 has a body-centered cubic (bcc) bixbyite structure with the space group $Ia\bar{3}$ [9]. The unit cell has 32 Er and 48 O atoms and the Er atoms occupy two different symmetry sites: C_2 and C_{3i}. A total of 8 Er atoms occupy

the C_{3i} site and the other 24 occupy the C_2 site. All of the photoluminescence described in this thesis came from Er^{3+} at the C_2 lattice site. This is because the C_{3i} retains inversion symmetry and electric dipole emission is forbidden. Magnetic dipole emission does occur [42] but not for any of the transitions considered in this thesis. As such, this thesis will only discuss the C_2 lattice site.

The sample used in the experiments described in Chapter 3 is a single-crystal 93 nm thick Er_2O_3 film grown on Si(111) using molecular beam epitaxy. This sample is shown in Figure 2.5 along with a cartoon depiction. The growth and materials characterization were done by a collaborator and are reported in Dodson et. al [2].

Figure 2.5: (left) Sample of Er2O3 used in this thesis. (right) Cartoon depiction of the sample.

CHAPTER 3

Photoluminescence from Er^{3+} in Er_2O_3

3.1 Overview and Experimental Setup

As a prelude to moving the existing theory forward in Chapter 4, we report our observations of the temperature dependence of the transition manifolds $^4S_{3/2} \rightarrow {}^4I_{15/2}$, $^4S_{3/2} \rightarrow {}^4I_{13/2}$ and $^2H_{11/2} \rightarrow {}^4I_{15/2}$ under 532 nm excitation. The discussion will begin with the experimental setup and methods, followed by the experimental observations and our analysis of those observations.

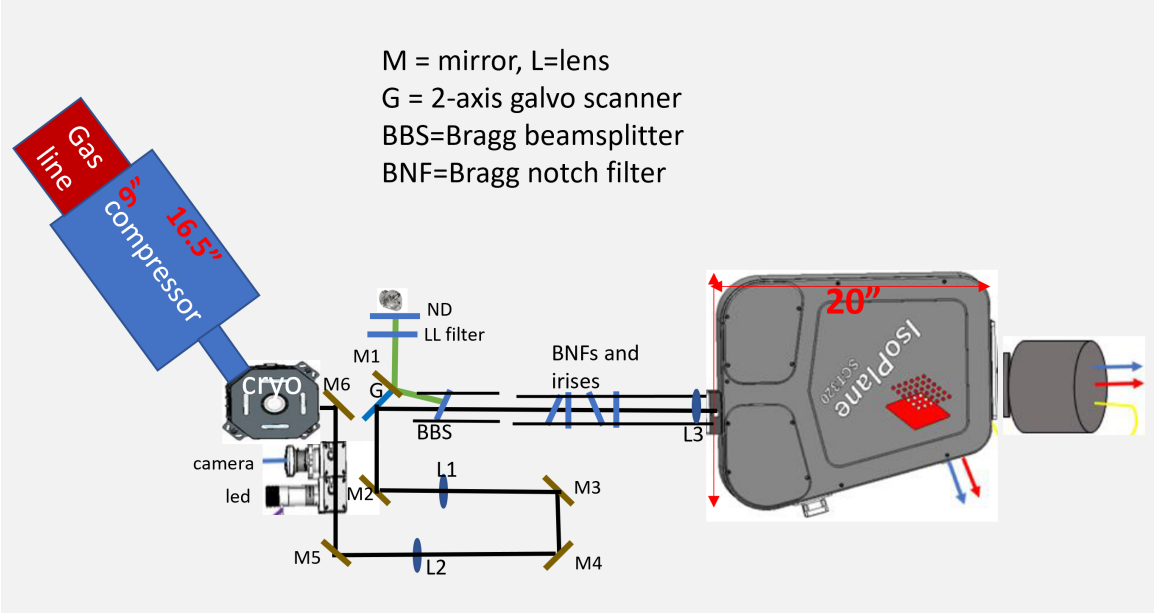

Figure 3.1: A schematic of the optics train used in the experiments. Reproduced from [2].

The measurement setup and experimental procedure were described in [2] and for completeness, we describe them again here in similar terms. We used a homebuilt confocal microscope in a Montana Instruments CryoStation equipped with a Zeiss LD EC Epiplan-Neofluar 100x DIC M27 objective (0.85NA) in order to vary the sample temperature between 4 K and 300 K. The excitation source was a Cobolt Samba CW 532 nm laser, measured to be 532.03±0.03 nm with a bandwidth <1 MHz (<3.3e-5 cm^{-1}). The reported

photoluminescence spectra were acquired with an IsoPlane SCT 320 spectrometer using a 600 lines/mm and 2400 lines/mm grating with a Pixis 400BR eXcelon camera. Bragg filters were used to acquire spectra within 10 cm^{-1} of the laser line, including a Bragg dichroic beamsplitter and two Bragg filters in the collection optics with associated irises used to suppress residual laser light. A schematic of the optics train is shown in Figure 3.1.

We collected the temperature dependent photoluminescence data using the following procedure. The Montana CryoStation was cooled to 4 K with the sample mounted inside. With the temperature stabilized, the laser was focused on the surface of the sample. This was confirmed by using a beam splitter to redirect some intensity onto a camera. This beam splitter is removed, and the photoluminescence data is collected. After completing the data collection at a given temperature the focus was checked to ensure stability through the duration of the measurement. Measurements were repeated in the rare event that the focus drifted. The sample was then warmed to the next temperature and the process described above was repeated. We took data at 10 K increments up to 300 K and reproduced the data at several different locations on the sample over the course of several months to ensure the reliability of the data.

3.2 Observed Temperature Dependent Photoluminesence

3.2.1 Transition Manifolds

Figure 3.2 shows the spectra of the transition manifolds $^4S_{3/2} \rightarrow {}^4I_{15/2}$, $^4S_{3/2} \rightarrow {}^4I_{13/2}$ and $^2H_{11/2} \rightarrow {}^4I_{15/2}$ between the temperatures of 4 K and 300 K. Within each transition manifold there are numerous spectral lines that originate from individual Stark-Stark transitions. As noted in Chapter 2, each $^{2S+1}L_j$ level is split into (j+1/2) Stark-split levels. Using the example of the $^4S_{3/2} \rightarrow {}^4I_{15/2}$ transition manifold, there will be a total of 2 excited Stark-split levels and 8 ground state Stark-split levels. Therefore, this manifold will contain 16 individual, often overlapping, spectral lines.

In order to compare the temperature dependent behavior of each manifold, we integrate

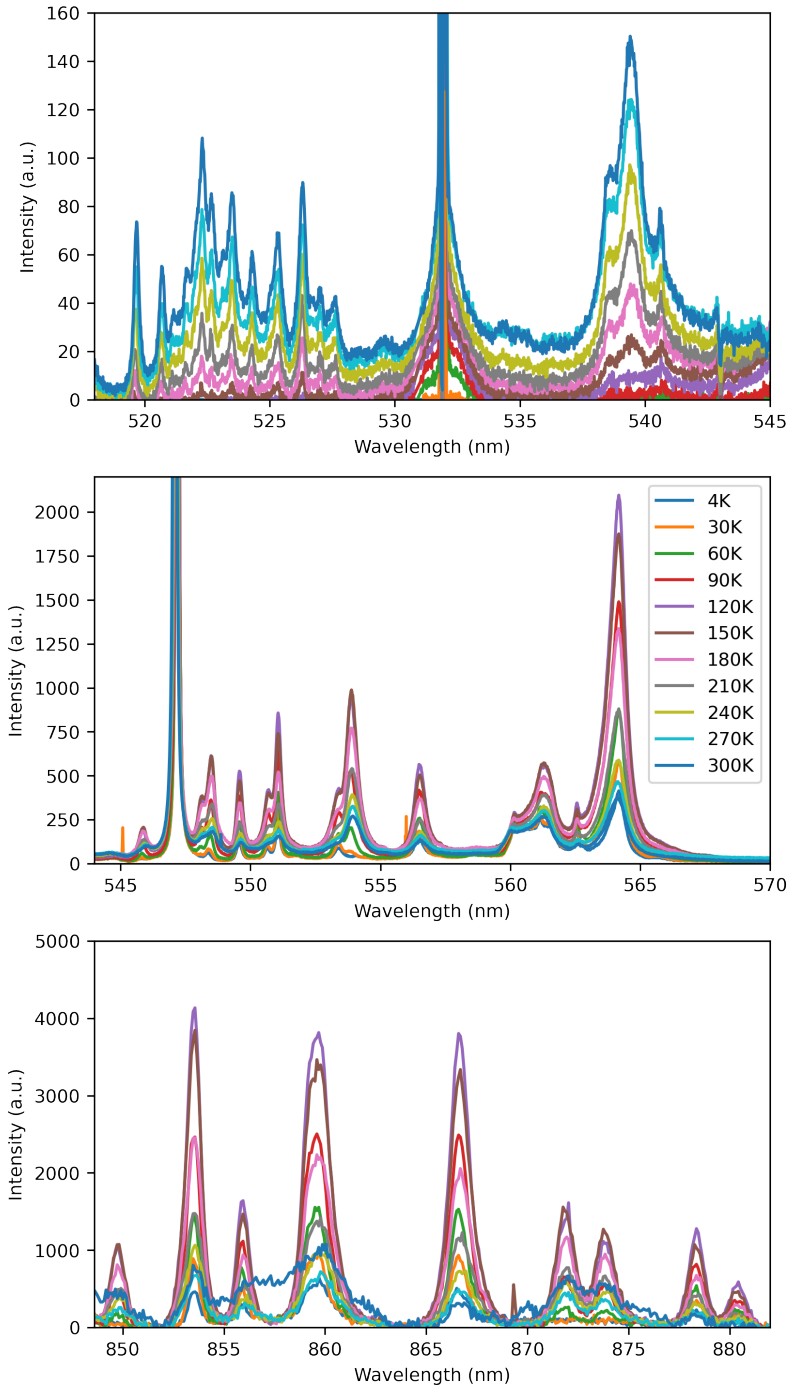

Figure 3.2: Observed Photoluminescence from the transition manifolds $^2H_{11/2} \rightarrow {}^4I_{15/2}$, $^4S_{3/2} \rightarrow {}^4I_{15/2}$ and $^4S_{3/2} \rightarrow {}^4I_{13/2}$ (middle) between the temperatures of 4 K and 300 K plotted at intervals of 30 K. The legend for $^4S_{3/2} \rightarrow {}^4I_{15/2}$ is shared amongst the 3 panels.

over each manifold and normalize to the maximum value observed over the measured temperature range. This normalization is necessary because the absolute intensities of these transitions vary over several orders of magnitude. The integrated photoluminescence data is plotted in Figure 3.3. From the data in Figure 3.3, it is evident that the temperature dependent behavior of $^4S_{3/2} \rightarrow {}^4I_{15/2}$ and $^4S_{3/2} \rightarrow {}^4I_{13/2}$ is virtually identical and suggests that the temperature dependent behavior of a transition manifold is determined only by the initial state.

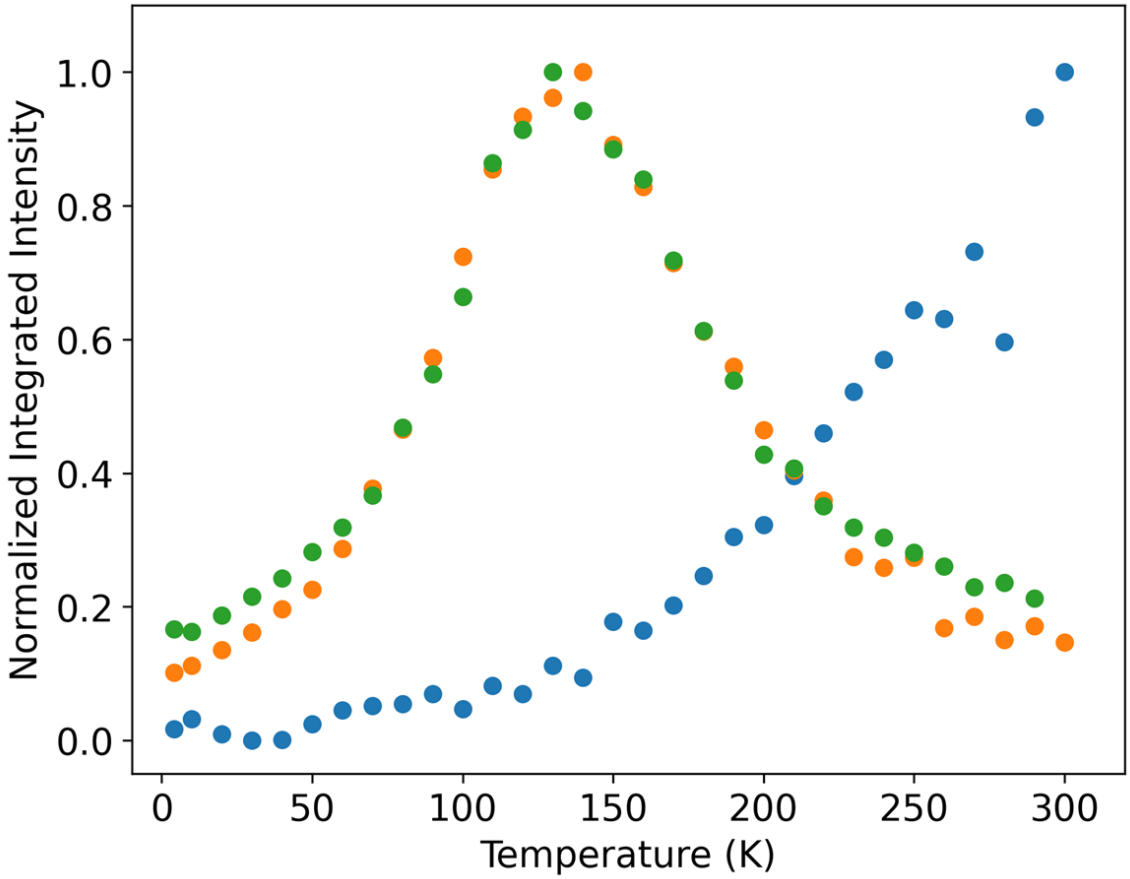

Figure 3.3: Integrated photoluminescence from $^4S_{3/2} \rightarrow {}^4I_{15/2}$ (orange), $^4S_{3/2} \rightarrow {}^4I_{13/2}$ (green) and $^2H_{11/2} \rightarrow {}^4I_{15/2}$ (blue). Adapted from [2].

3.2.2 Temperature Dependence of Stark-Stark Transitions

This analysis of the temperature dependence can be extended to the transitions between individual Stark-split levels within the transition manifolds. At every temperature, well-

separated spectral lines were fit to a Lorentzian lineshape of the form:

$$L(\lambda) = \frac{h}{2\pi} \frac{\Gamma}{(\lambda - \lambda_0)^2 + \left(\frac{1}{2}\Gamma\right)^2} + y_0, \tag{3.1}$$

where Γ is the linewidth of the Lorentzian, λ_0 is the center wavelength of the transition, h is a rescaling factor and y_0 is a vertical offset. All were permitted to be fit parameters, however, λ_0 was constrained to remain within 0.1 nm of the wavelength values calculated from the energy levels reported by Gruber et. al.

In several cases, there were two nearly overlapping spectral lines. Those where fit to a sum of Lorentzian lineshapes of the form:

$$L(\lambda) = \frac{h_1}{2\pi} \frac{\Gamma_1}{(\lambda - \lambda_{01})^2 + \left(\frac{1}{2}\Gamma_1\right)^2} + \frac{h_2}{2\pi} \frac{\Gamma_2}{(\lambda - \lambda_{02})^2 + \left(\frac{1}{2}\Gamma_2\right)^2} + y_0, \tag{3.2}$$

where the variables are defined above, and the additional subscripts are associated with one of the overlapping spectral lines.

Once again, to compare the temperature dependent behavior of each spectral line, the fit values for h of each spectral line were normalized to the maximum value observed over the measured temperature range. This is plotted in Figure 3.4b,c. The specific Stark-Stark transitions are noted on an energy level diagram in Figure 3.4a. What is evident from Figure 3.4b is that the temperature dependence of individual Stark-Stark lines originating from the $^4S_{3/2}$ level is grouped by the Stark level of origin. Based on Figure 3.4, we can assume the same holds true for the Stark-Stark lines originating from the $^2H_{11/2}$ level, although it is not quite as evident. The close spacing of the spectral lines of the $^2H_{11/2} \rightarrow {}^4I_{15/2}$ transition manifold made a clearer determination difficult, but it assumed to be the case.

3.2.3 Origin of the Observed Temperature Dependence

The photon emission rate from an excited state is given by:

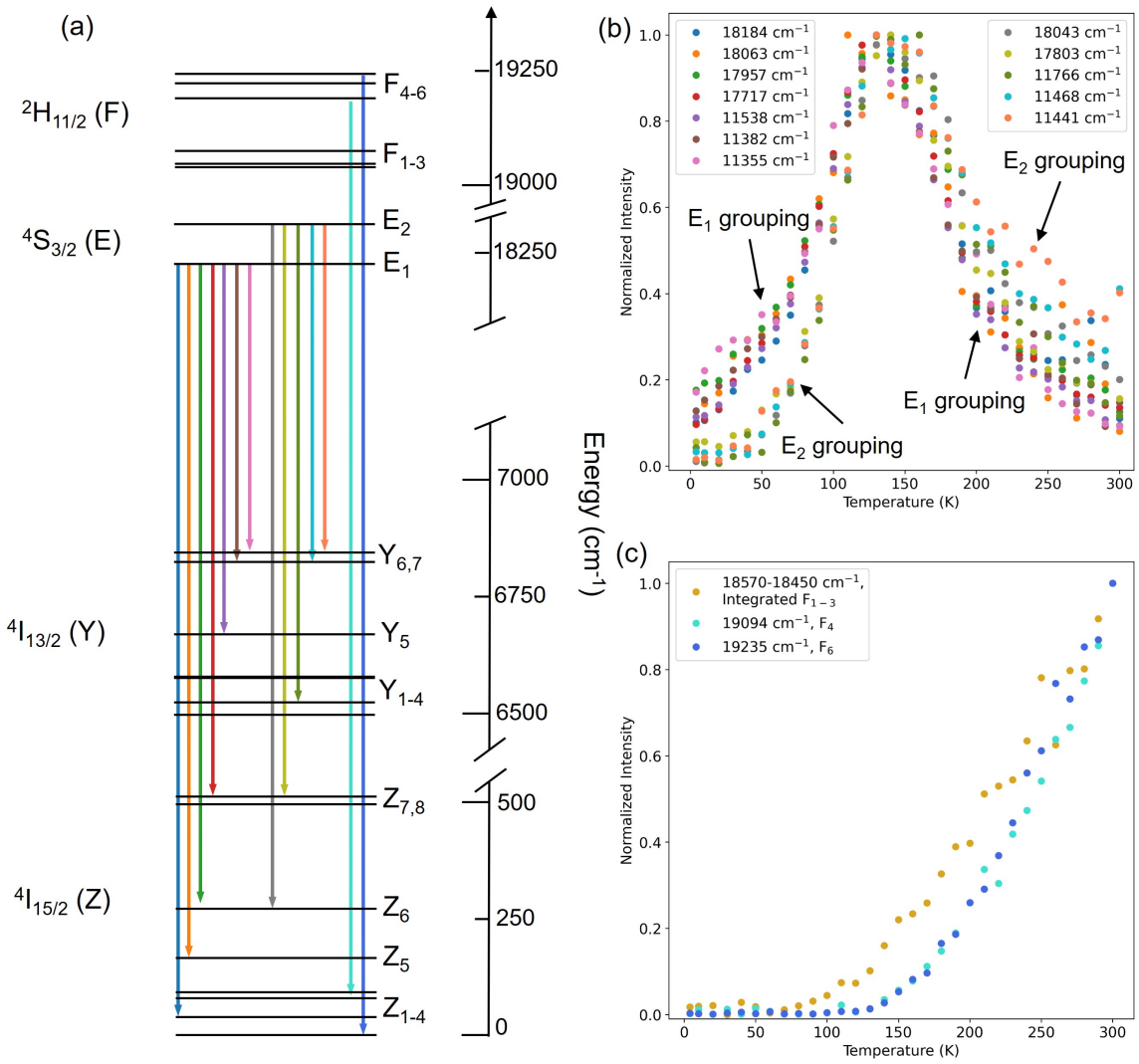

Figure 3.4: (a) Er^{3+} level diagram showing the splitting of $^2H_{11/2}$, $^4S_{3/2}$, $^4I_{13/2}$ and $^4I_{15/2}$ due to the crystal field of Er_2O_3. Also shown are representative transitions. The transition lines are color-coded to the data shown in (b) and (c). Normalized temperature dependent intensity of peaks originating from several excited Stark-split levels in $^4S_{3/2}$ (b) and $^2H_{11/2}$ (c). Once normalized, the temperature dependent behavior was identical for photoluminescence peaks originating from the same Stark-split level. Adapted from [2].

$$I_i = A_i N_i, \tag{3.3}$$

where A_i is the spontaneous emission rate and N_i is the level population fraction. Based on the data presented above, we can conclude that the dominant driver of the temperature

dependence of photoluminescence from Er^{3+} in Er_2O_3 is the temperature dependence of the level population fraction, N_i, of the individual Stark level. With this conclusion, in Chapter 4, we will expand the theoretical basis for modeling the observed temperature dependence discussed in this chapter that expands upon the established theory for non-resonant excitation of rare-earth ions. Then in Chapter 5 we apply the model to the observed temperature dependent data shown in this chapter and discuss the implications of the model output.

CHAPTER 4

Modeling Temperature Dependent Photoluminescence

Laser-driven excitation of rare-earth ions is relevant for multiple applications. Non-resonant excitation is common and needs to be understood to be exploited for applications such as optical thermometry [6; 8]. The theory of non-resonant excitation of rare-earth ions is well-established but the typical approach makes assumptions that can break down at reduced temperatures ($<$150 K). Here, we advance the theory to properly model our observations over the temperature range from 4 K to 300 K. First, we will consider the Stark-split levels of the rare-earth ion rather than treating each Stark-split manifold as a single unit. Second, this consideration of the Stark-split levels will allow us to incorporate both Stokes and anti-Stokes excitations into our model instead of a single anti-Stokes excitation, which is unable to explain non-resonant photoluminescence below $\sim$100 K. Finally, this will permit us to incorporate material-specific phonon energies rather than a single effective phonon energy, which is an approach that works well only at elevated temperatures. As will be shown in Chapter 5, these extensions of existing theory allow us to explain the temperature dependence of the observed photoluminescence between 4 K and 300 K.

4.1 Photoluminescence

As stated in Chapter 3, the photon emission rate from an excited state is given by:

$$I_i = A_i N_i, \tag{4.1}$$

where A_i is the spontaneous emission rate and N_i is the level population. From the discussion in Chapter 3, the spontaneous emission rate is weakly dependent on temperature and the temperature dependence of level population fraction, N_i, is the main source of the observed temperature dependence of the photoluminescence.

Under steady state excitation, the temperature dependence of N_i can be attributed to three distinct temperature-dependent processes. First, the thermalization of the Er^{3+} ion between the closely space Stark-split levels of the excited states $^2H_{11/2}$ and $^4S_{3/2}$ as well as the ground state $^4I_{15/2}$. Second, the temperature dependence of the phonon-assisted excitation cross sections which permit Er^{3+} ions to be excited out of the ground state. Finally, the temperature-dependent excited state lifetime that results from the thermal coupling of the $^2H_{11/2}$ and $^4S_{3/2}$ levels, which have different intrinsic lifetimes. In what follows, we quantify these three temperature-dependent processes.

4.2 Thermalization

4.2.1 Excited and Ground State Thermalization

The Stark-split levels of Er^{3+} in Er_2O_3 are sufficiently close that a collection of Er^{3+} ions in a given level of the $^{2S+1}L_j$ states can be described by a Boltzmann distribution. This fact is often exploited in using rare-earth ions, including Er^{3+}, in optical thermometry [6; 7; 21; 46; 47]. Here we will present experimental evidence for the thermalization of the excited states $^4S_{3/2}$ and $^2H_{11/2}$ and discuss the validity of extending that assumption to the ground state $^4I_{15/2}$.

The typical method to demonstrate that two excited states are in thermal equilibrium is that the ratio of luminescence from the states can be described by an equation of the form [48]:

$$\frac{I_2}{I_1} = Ae^{-E_{21}/k_bT}, \tag{4.2}$$

where I_1 and I_2 are the intensities of the two levels, A is a fitting constant and E_{21} is the energy difference between the levels. The ratio of luminescence from the $^2H_{11/2}$ and the $^4S_{3/2}$ levels is plotted in Figure 4.1. The fit line is equation 4.2 using E_{21} = 863 cm^{-1}, which is the difference between the center of gravity energies of these levels [1]. It is clear from Figure 4.1 that the ratio of the luminescent intensities from 4 K to 300 K is

well described by Equation 4.2. Therefore, Er^{3+} ions in these two levels are in thermal equilibrium and by extension the individual Stark-split levels are as well.

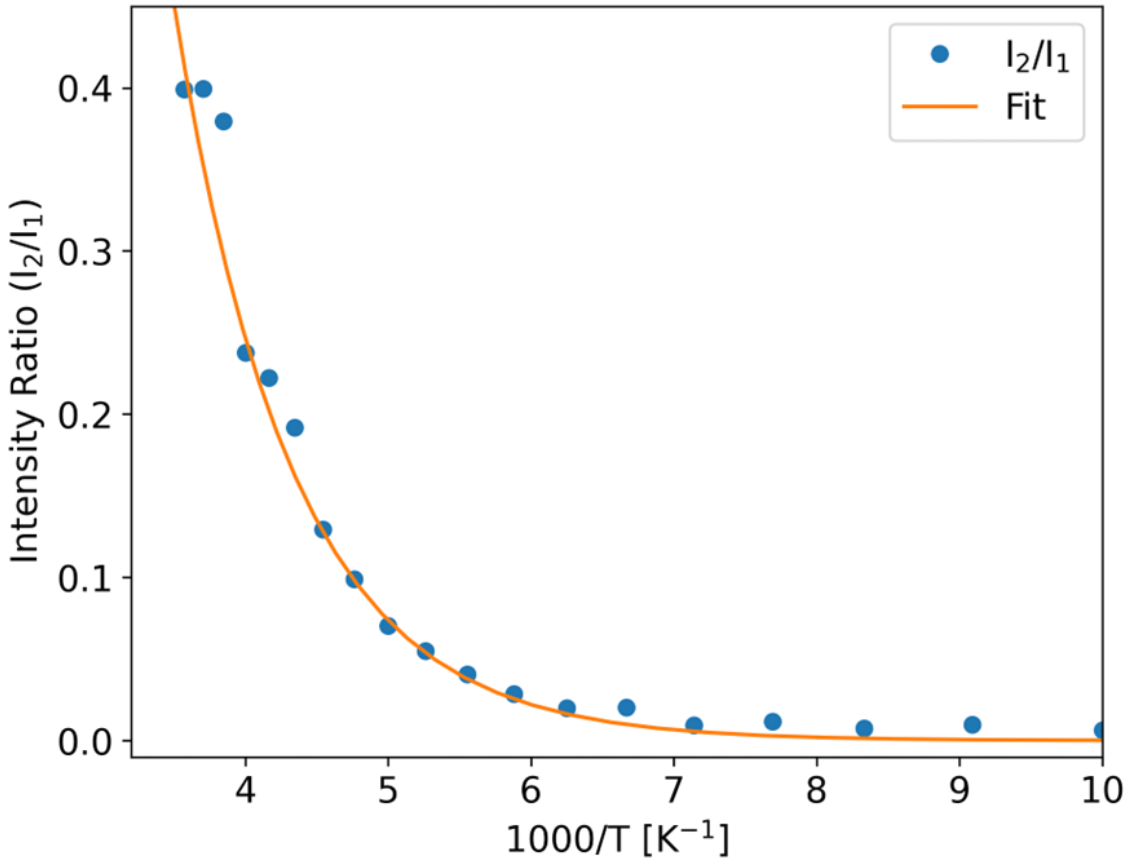

Figure 4.1: Ratio of the integrated photoluminescence from $^2H_{11/2}$ and $^4S_{3/2}$ (blue dots). The fit line is Equation 4.2 using E_{21} = 863 cm^{-1}. Adapted from [2]

This assumption of thermal equilibrium can be extended to a collection of Er^{3+} ions in the ground state $^4I_{15/2}$. While we have made no direct measurement, a comparison between the energy spread of the ground state $^4I_{15/2}$ and E_{21} is sufficient to support the assumption. The difference in energy between the lowest lying and highest lying Stark-split states of the Er^{3+} ground state $^4I_{15/2}$ is 505 cm^{-1}. This is less than E_{21}, therefore it is reasonable to assume that a collection of Er^{3+} ions in the ground state are in thermal equilibrium and can be described by a Boltzmann distribution. We now quantify these statements.

The population of Er^{3+} ions in each of the ground state Stark levels is given by:

$$N_{Z_i}(T) = N_g P_{Z_i}(T), \tag{4.3}$$

where N_g is the total population fraction of Er^{3+} ions in the ground state $^4I_{15/2}$, and P_{Z_i}(T) is the thermal probability of an Er^{3+} ion being in the Z_i state of $^4I_{15/2}$. Similar statements can be written for the Stark-split levels of the excited states $^2H_{11/2}$ (F), and $^4S_{3/2}$ (E):

$$N_{F_i}(T) = N_e P_{F_i}(T), \tag{4.4}$$

$$N_{E_i}(T) = N_e P_{E_i}(T), \tag{4.5}$$

where N_e is the total population fraction of Er^{3+} ions in the excited states, $^2H_{11/2}$ and $^4S_{3/2}$. Then P_{F_i}(T) and P_{E_i}(T) are the thermal probabilities of an Er^{3+} ion being in the F_i state of $^2H_{11/2}$ and E_i state of $^4S_{3/2}$, respectively.

The definitions for P_{Z_i}(T), P_{F_i}(T) and P_{E_i}(T) are as follows:

$$P_{Z_i}(T) = \frac{exp\left(\frac{-\varepsilon_{Z_i}}{kT}\right)}{\sum_{n=1}^{8} exp\left(\frac{-\varepsilon_{Z_n}}{kT}\right)}, \tag{4.6}$$

$$P_{F_i}(T) = \frac{exp\left(\frac{-\varepsilon_{F_i}}{kT}\right)}{\sum_{n=1}^{6} exp\left(\frac{-\varepsilon_{F_n}}{kT}\right) + \sum_{m=1}^{2} exp\left(\frac{-\varepsilon_{E_m}}{kT}\right)}, \tag{4.7}$$

$$P_{E_i}(T) = \frac{exp\left(\frac{-\varepsilon_{E_i}}{kT}\right)}{\sum_{n=1}^{6} exp\left(\frac{-\varepsilon_{F_n}}{kT}\right) + \sum_{m=1}^{2} exp\left(\frac{-\varepsilon_{E_m}}{kT}\right)}, \tag{4.8}$$

where ε_{Z_i},ε_{F_i},ε_{E_i} are the energies of the Stark-split levels in $^4I_{15/2}$, $^2H_{11/2}$ and $^4S_{3/2}$ respectively. These energies are given in Table 2.1. The partition function in the denominator of Equations 4.6 - 4.8 are set by the levels in thermal equilibrium. In the case of the excited state Stark-split levels of $^4S_{3/2}$ and $^2H_{11/2}$, Er^{3+} ions equilibrate among all 8 Stark-split

levels and the partition function reflects that. Figure 4.2 shows the values of $P_{Z_i}(T)$, $P_{F_i}(T)$ and $P_{E_i}(T)$ over the experimental temperature range (4 K to 300 K).

4.2.2 Temperature Dependent Lifetime

The thermal coupling of the excited states $^2H_{11/2}$ and $^4S_{3/2}$ results in a temperature dependent lifetime for the excited states. We explicitly assume that the intrinsic excited state lifetime of the individual Stark-split states is independent of temperature. Given the minimal change in Stark splitting over the temperature range from 4 K and 300 K [31], the radiative lifetimes depend weakly on temperature. This is further supported by the observation that the dominant driver of the temperature dependence in Equation 4.1 is the temperature dependence of the population fraction N_i which suggests that the transition probabilities change little with temperature. The same is assumed for the nonradiative lifetimes, although it is unlikely to be true. An additional complication is that these lifetimes are likely to vary between individual Stark-split levels of the excited state. However, both of these complications are beyond the scope of this thesis. We define the intrinsic excited state lifetime for the individual Stark-split levels of $^2H_{11/2}$ as τ_F and of $^4S_{3/2}$ as τ_E.

We now give an expression for the temperature dependence of the excited state lifetime, $\tau(T)$, that results from the thermal coupling of the $^2H_{11/2}$ and $^4S_{3/2}$ states. Due to thermalization, an Er^{3+} ion in the excited state has numerous effective pathways to the ground state and the contribution of each pathway is simply the thermal probability of the Er^{3+} ion being in that state at any given temperature. Therefore, the $\tau(T)$ is given by:

$$\frac{1}{\tau(T)} = \frac{\sum_i P_{F_i}(T)}{\tau_F} + \frac{\sum_i P_{E_i}(T)}{\tau_E} = \frac{\tau_E \sum_i P_{F_i}(T) + \tau_F \sum_i P_{E_i}(T)}{\tau_F \tau_E}, \tag{4.9}$$

where all variables have been defined previously. Equation 4.9 is plotted over the experimental range (4 K to 300 K) in Figure 4.3. Having now established the temperature dependent behavior of Er^{3+} ions in both the excited state and ground state as well as the decay from the excited state to the level of individual Stark-split states, we turn our atten-

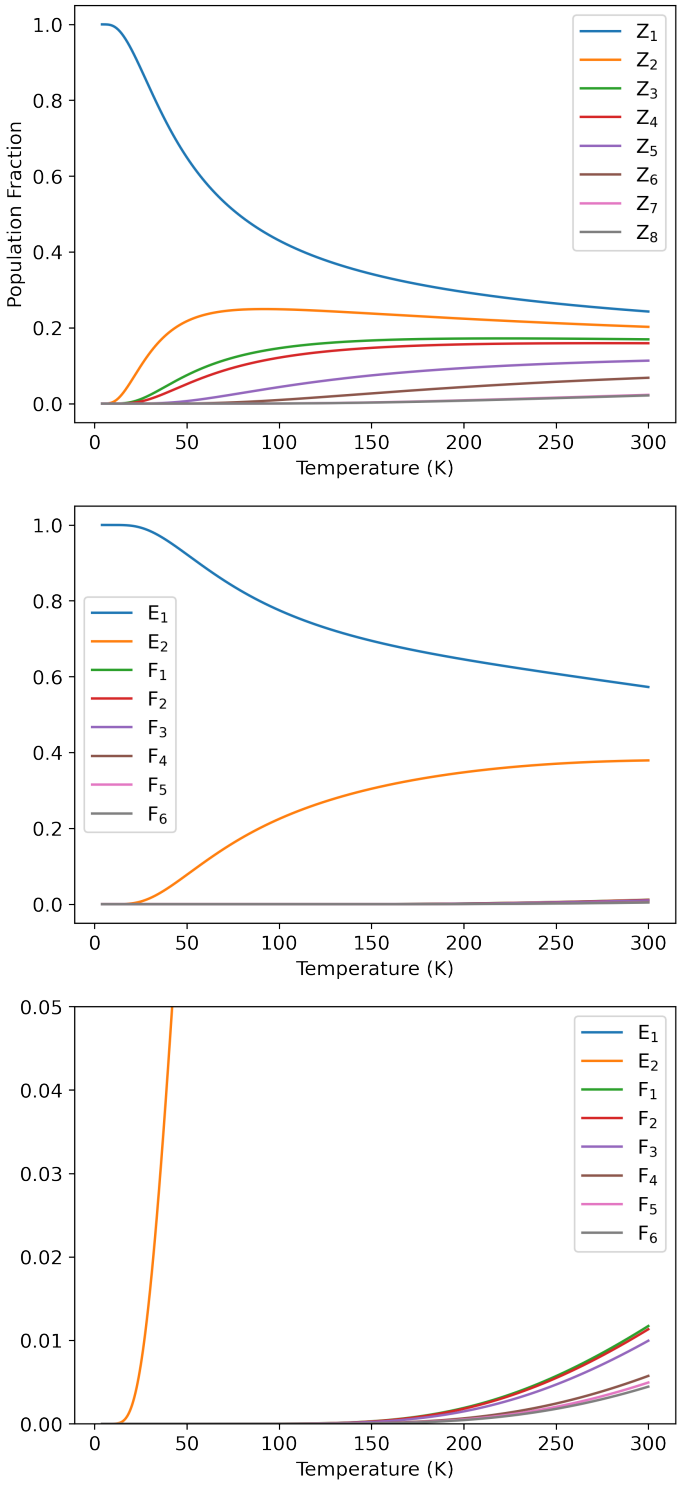

Figure 4.2: Population fractions $P_{Z_i}(T)$ for the ground state Stark-split levels of $^4I_{15/2}$ (top). Population fractions $P_{F_i}(T)$ and $P_{E_i}(T)$ for the ground state Stark-split levels of $^2H_{11/2}$ and $^4S_{3/2}$ respectively (middle, zoomed bottom). Adapted from [2]

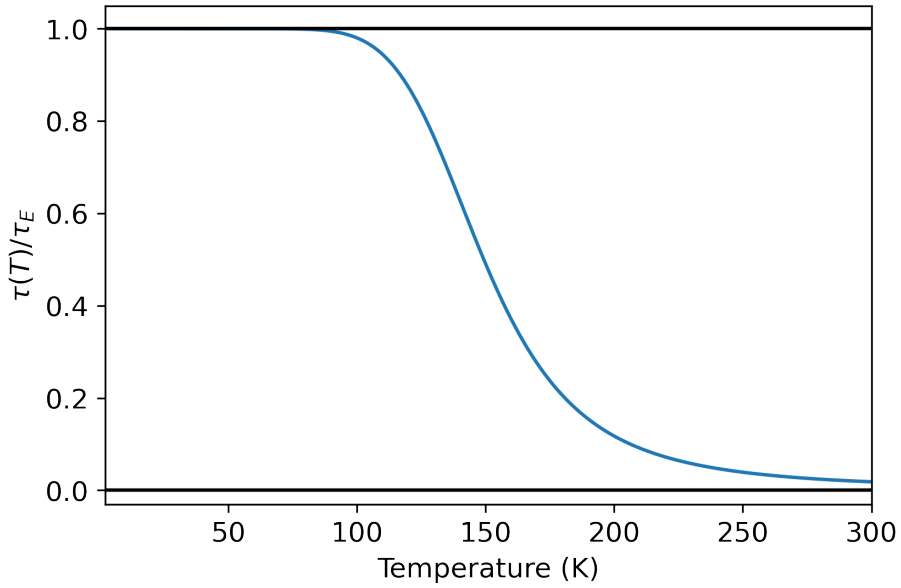

Figure 4.3: Variation in $\tau(T)$ as a function of temperature, normalized to τ_E. The black lines represent τ_E/τ_E and τ_F/τ_E, respectively.

tion to establishing the temperature dependence of non-resonant excitation at the level of individual Stark-split states.

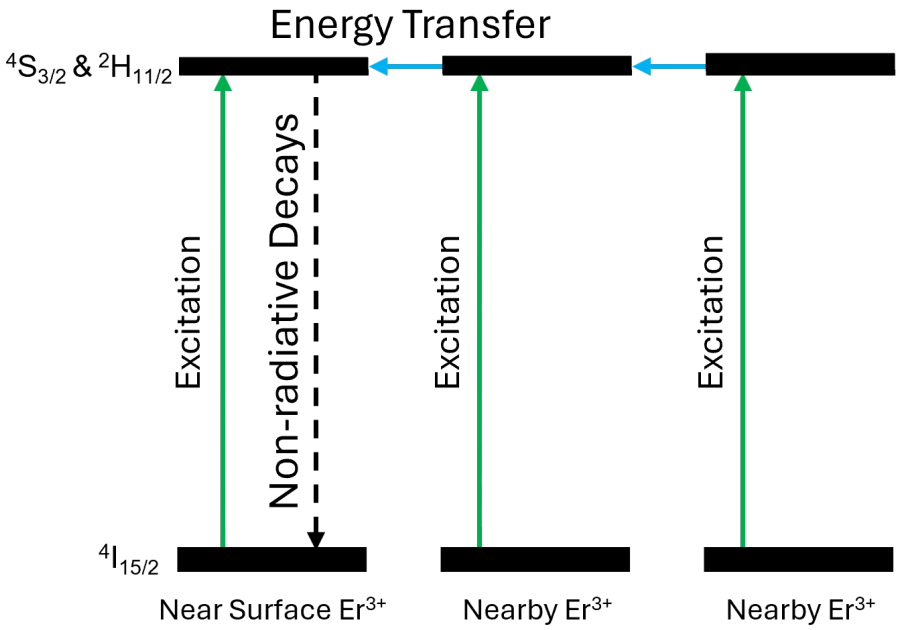

Figure 4.4: Schematic of the proposed mechanism for the quenching of Er^{3+} photoluminescence in thin films of Er_2O_3

4.2.3 Interface Effect

Recent unpublished work has shown the possibility that there is an additional non-radiative decay pathway that results from the interface of Er_2O_3 with the Si substrate and/or the surface of Er_2O_3. This additional non-radiative pathway allows the Er^{3+} ions near the interface/surface to decay non-radiatively significantly faster than any radiative pathway. Then, through resonant energy transfer between nearby Er^{3+} ions, the near interface Er^{3+} ions are re-excited, deexciting the nearby Er^{3+} ion. The near surface/interface Er^{3+} ions again decay non-radiatively. This process is continues until all the Er^{3+} ions throughout the film return to the ground state, fully quenching any radiative emission from Er^{3+}. A schematic of this effect is shown in Figure 4.4.

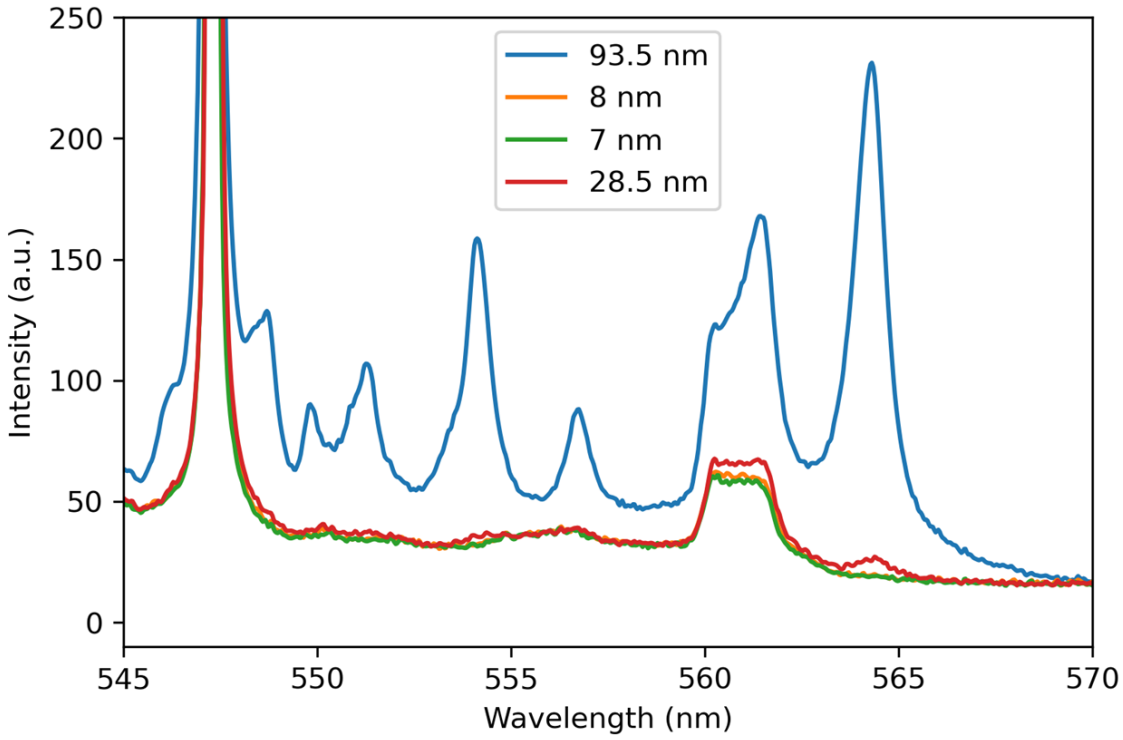

Figure 4.5: Variation of the $^4S_{3/2} \rightarrow {}^4I_{15/2}$ as a function of the thickness of the Er_2O_3 film.

Photoluminescence from the $^4S_{3/2} \rightarrow {}^4I_{15/2}$ of Er^{3+} in Er_2O_3 films of thicknesses ranging from 7 nm to 93 nm are shown in Figure 4.3. This photoluminescence is conducted at room temperature using a 532 nm laser. Based on Figure 4.3, all emission is quenched be-

low a thickness of ∼28 nm. A complete accounting of this effect, including the temperature dependence, is not yet known and is therefore neglected in Equation 4.9 despite its likely contribution to the overall temperature dependent lifetime in thicker samples. Regardless of this omission, the effect has implications for any applications involving nanostructures incorporating Er^{3+} ions which place those ions near surfaces/interfaces.

4.3 Temperature Dependent Excitation

4.3.1 Stokes and anti-Stokes Excitation

The rate of laser-drive excitation between a ground state and an excited state takes the general form of:

$$W_{exc} = \frac{\sigma I}{h\nu} N_g, \tag{4.10}$$

Where N_g is the ground state population, σ is the excitation cross section, I is the laser intensity and $h\nu$ is the photon energy of the incident light. In the present case, the temperature dependence of W_{exc} comes from the temperature dependence of the phonon-assisted excitation cross section σ(T) and the thermalization of the ground state Stark levels. The former contributes to the temperature dependence only in the case of non-resonant excitation, while the latter always occurs. The thermalization of the ground state Stark levels was discussed above. Here we will discuss the phonon-assisted excitation cross section from both anti-Stokes and Stokes excitation.

Generic phonon-assisted anti-Stokes and Stokes excitation occurs when the incident wavelength of excitation, commonly a laser, is non-resonant with the transition energy. When the excitation source is non-resonant with the transition, a phonon can be absorbed from the material (Stokes) or emitted into the material (anti-Stokes) to make up the difference in energy. For the case of rare-earth ions, anti-Stokes and Stokes excitation occur in the weak-coupling ion-lattice regime [18]. The temperature dependent cross sections, σ_{AS}(T) and σ_S(T) for anti-Stokes and Stokes excitation, respectively, take on the general

form of:

$$\sigma_{AS}(T) = S_0^p \sigma_{res} \left(e^{\frac{\varepsilon}{k_b T}} - 1 \right)^{-p}, \tag{4.11}$$

$$\sigma_{AS}(T) = S_0^p \sigma_{res} \left(1 - e^{\frac{-\varepsilon}{k_b T}} \right)^{-p}, \tag{4.12}$$

where ε is the phonon energy, S_0 is the Pekar-Huang-Rhys coupling constant, σ_{res} is the resonance cross section of the transition and p is the number of phonons of energy ε assisting the transition [18; 19; 27; 28; 34]. The temperature dependence of both cross sections is given in Figure ?, with p=S_0=σ_{res}=1 and ε_l = 316.4 cm^{-1} - one of the phonon energies in Er_2O_3. It is important to note that while the temperature dependence of both Stokes and anti-Stokes is the same, the non-zero offset of the Stokes transitions at reduced temperatures means that any observed emission near 0 K is a direct consequence of only Stokes excitations.

In what follows, we will introduce additional prefactors to Equations 4.11 and 4.12 and set p=1 consistent with experimental observations and existing literature [27]. The final form is:

$$\sigma_{AS}(T) = S_0 g_p \sigma_{ij,res} f_{bw,l} \left(e^{\frac{\varepsilon_l}{k_b T}} - 1 \right)^{-1}, \tag{4.13}$$

$$\sigma_{AS}(T) = S_0 g_p \sigma_{ij,res} f_{bw,l} \left(1 - e^{\frac{-\varepsilon_l}{k_b T}} \right)^{-1}, \tag{4.14}$$

where g_p is the degeneracy of the phonon mode l, $\sigma_{ij,res}$ is the resonance cross section of the transition between subscripted levels, ε_l is the energy of phonon mode l, $f_{bw,l}$ is a factor to account for the mismatch between Er_2O_3 phonon energies and the energy required to facilitate a phonon-assisted transition at the incident laser energy. It is defined below. All other variables have been defined previously. In what follows, each additional factor of

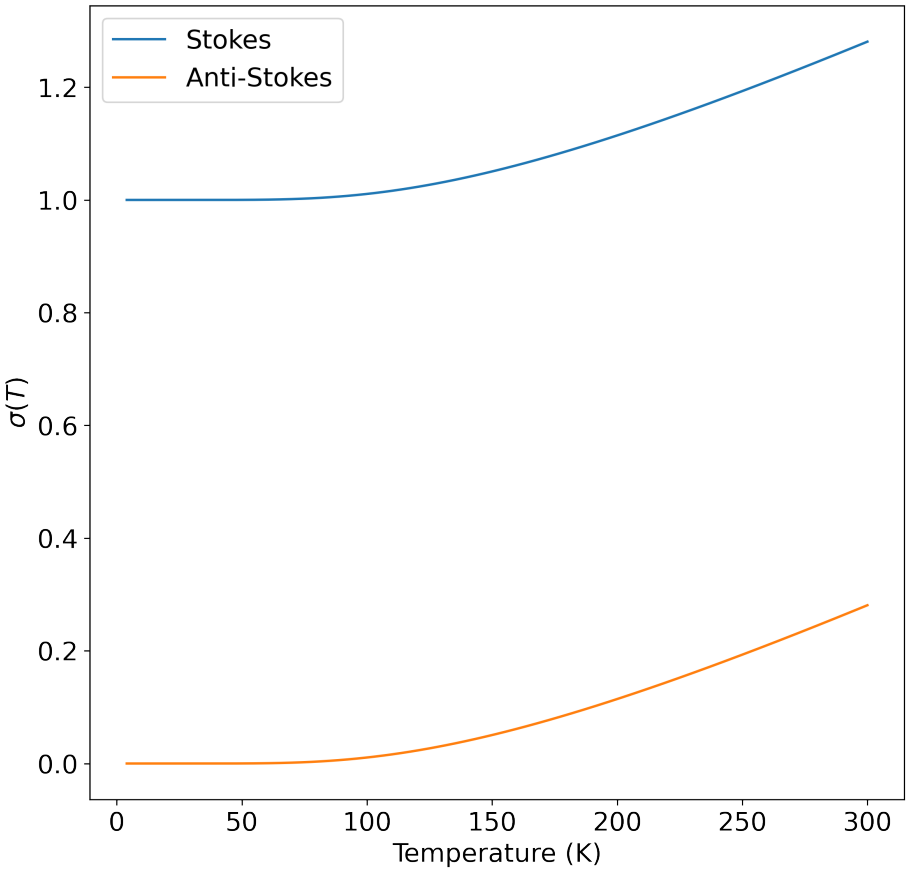

Figure 4.6: Temperature dependence of Stokes and anti-Stokes transitions between 4 K and 300 K for a phonon energy of 316.4 cm^{-1}

Equations 4.13 and 4.14 is discussed.

4.3.2 Pekar-Huang-Rhys Constant

The Pekar-Huang-Rhys coupling constant, S_0, characterizes the electron-phonon coupling in a system. This constant quantifies the change in lattice equilibrium between the ground and excited states. An upper bound for S_0 in a rare-earth system can be estimated from observed photoluminescence spectra in the following way. The ratio of the probabilities between the zero-phonon line (P(0,T)) and single phonon line (P(1,T)) at a given temperature is given by [19]:

$$\frac{P(0,T)}{P(1,T)} = \frac{1}{S_0(\bar{n}+1)} \tag{4.15}$$

where $\bar{n}$ is the occupation number of the mode with energy ε_l and is given by:

$$\bar{n} = \left(e^{\frac{\varepsilon_l}{kT}} - 1\right)^{-1}. \tag{4.16}$$

At 300 K, $\bar{n} \approx 2$ for the lowest energy phonon in Er_2O_3, therefore:

$$\frac{P(0,300K)}{P(1,300K)} = \frac{1}{3S_0}. \tag{4.17}$$

There are no phonon replica peaks evident in the spectra at 300 K. Based on the noise level that allows us to constrain $S_0 \leq 0.01$. This is consistent with the typical value of S_0 for rare earth ions in materials is ~0.02-0.04. From Equation 4.11 and 4.12, it is obvious that single-phonon processes will dominate. Therefore, it is reasonable that we confine our focus to p=1, consistent with published work for the transition considered [27].

4.3.3 Finite Phonon Bandwidth

The term $f_{bw,l}$ is defined as follows:

$$f_{bw,l} = \frac{L_l(\Delta_{ij},\Gamma)}{L_l(\varepsilon_l,\Gamma)}, \tag{4.18}$$

where Δ_{ij} is the difference between the incoming phonon energy and the $i \rightarrow j$ Stark-Stark transition energy (see Table 4.1), ε_l is the center energy of the phonon, Γ is the energy bandwidth (FWHM) of the phonon and $L_l(\varepsilon,\Gamma)$ is the Lorentzian function centered at ε_l and defined as:

$$L_l(\varepsilon,\Gamma) = \frac{1}{2\pi}\frac{\Gamma}{(\varepsilon-\varepsilon_0)^2 + \left(\frac{1}{2}\Gamma\right)^2}, \tag{4.19}$$

A visual depiction of $f_{bw,l}$ and $L_l(\varepsilon,\Gamma)$ is given in Figure 4.7.

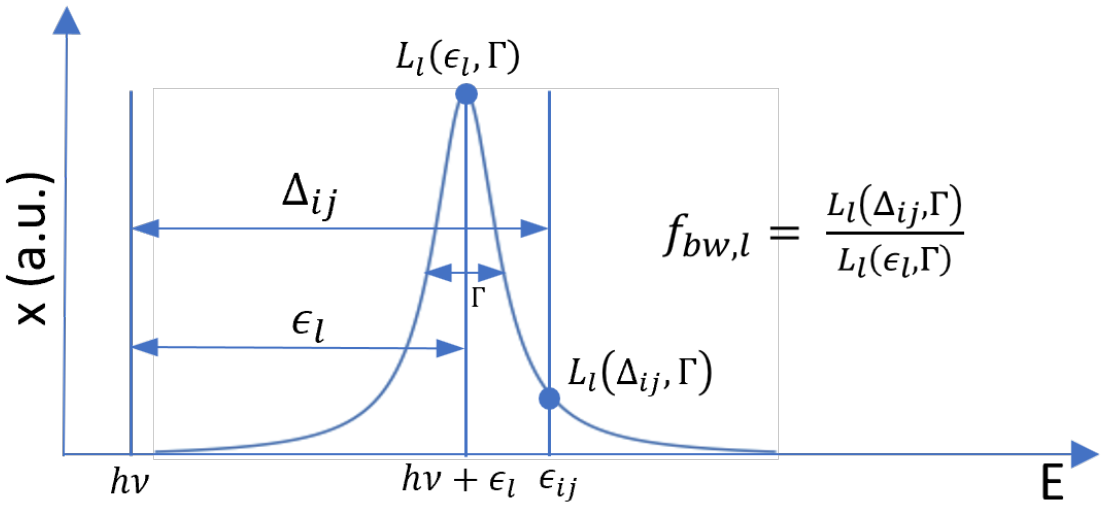

Figure 4.7: A schematic representation of $f_{bw,l}$. Reproduced from [2].

The factor, $f_{bw,l}$, is needed for two main reasons. First, phonons have finite lifetimes and therefore have finite energy bandwidths. By looking at a well-studied phonon mode in Lu_2O_3, which like Er_2O_3 is a rare-earth sesquioxide with C-type bixbyite structure, we can see that the linewidths of phonons are expected to be on the order of several cm^{-1} [49]. Therefore, phonon modes with energies that are close to matching the energy required to facilitate a Stokes/anti-Stokes can occur and the term $f_{bw,l}$ allows us to address that possibility. The second reason is an extension of the first. With 532.03 nm excitation, there are very few phonon energies in Er_2O_3 that closely match ($<$0.5 cm^{-1} difference) the energy required to facilitate a Stark-Stark transition from the ground state of Er^{3+}. If limited to only the so-called "close matches," there is negligible excitation and by extension negligible photoluminescence below 15 K. That is inconsistent with the observed data plotted in Figure 3.2 which clearly slows emission from the E_1 state of $^4S_{3/2}$. This inconsistency can be resolved by allowing the phonons of Er_2O_3 to have finite energy bandwidth. In what follows, we use observations to give a rough estimate for the phonon bandwidths in Er_2O_3.

At temperatures below 15 K, Equation 4.6 predicts that the ensemble of Er^{3+} ions will be in the lowest energy level of $^4I_{15/2}$, called Z_1. Therefore, any observed photolumines-

cence can only result from exciting Er^{3+} from this level. At these temperatures, there is no thermal bath of phonons, therefore any phonon-assisted excitation will be a Stokes transition. It can be shown that at the experimental excitation wavelength, there are two possible Stokes transitions: $Z_1 \rightarrow E_1$ and $Z_1 \rightarrow E_2$. At the incident wavelength, a phonon of energy 574 cm^{-1} is required for the former and one of 488 cm^{-1} is required for the latter. According to Table 4.1, the closes phonon energy in Er_2O_3 to 574 cm^{-1} is at 576.1 cm^{-1}, a shift of 2.1 cm^{-1}. The closest phonon energy to the required 488 cm^{-1} is at 494.3 cm^{-1}, a shift of 6.3 cm^{-1}. Therefore, if the phonons do not have a finite energy bandwidth, there is not a phonon of the correct energy in Er_2O_3 to facilitate either transition from Z_1 at these low temperatures. Therefore, to explain the observed photoluminescence at these temperatures the phonons of Er_2O_3 must have a finite energy bandwidth on the order of several cm^{-1}. To account for this and incorporate those transitions into a model consistent with conservation of energy, the term $f_{bw,l}$ is required.

4.3.4 Stark-Stark Resonance Cross Sections

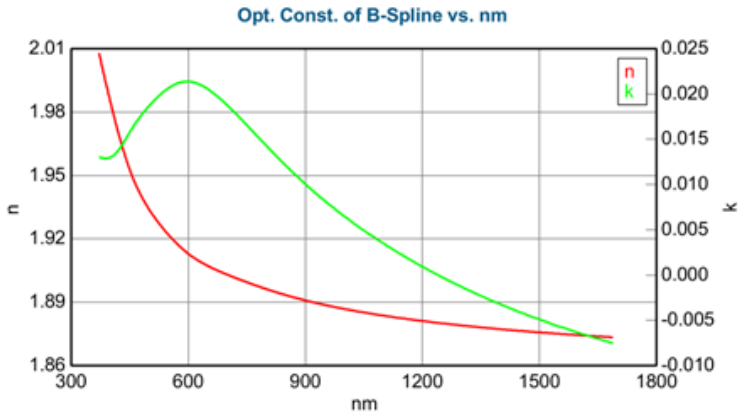

Figure 4.8: Fit of optical constants to ellipsometry data of the 93 nm thick Er_2O_3

To derive the resonance cross sections that will be used in the Equations 4.13 and 4.14, we use the method given in Aull, et.al. [50] and stated below in equation 4.20. It is important to note that the spectral variations of the host refractive index are negligible over the wavelengths for these transitions; an assumption necessary to use Equation 4.20.

Figure 4.8 shows the results of fitting ellipsometry data for the 93 nm thick Er_2O_3 film. The variation in the index of refraction, n, over several nanometers of wavelength is <0.01. Therefore, we can use the following relation between resonance cross sections:

$$\frac{I_{ji}(\nu)}{I_{j'i'}(\nu')} = \left(\frac{\nu}{\nu'}\right)^3 \frac{N_j}{N_{j'}} \frac{\sigma_{ji}}{\sigma_{j'i'}(\nu')}, \tag{4.20}$$

where I_{ji} is the fluorescent intensity of the $j \rightarrow i$ transition, ν is the frequency of the emitted light, N_j is the population density of j and $\sigma_{ji}(\nu)$ is the emission cross section for the $j \rightarrow i$ transition. The emission and absorption cross sections are related by:

$$\sigma_{ji}(\nu) = \left(\frac{g_i}{g_j}\right) \sigma_{ij}(\nu), \tag{4.21}$$

where $\sigma_{ji}(\nu)$ is the absorption cross section for $i \rightarrow j$ and g_i and g_j are the degeneracies of i and j respectively. All of the Stark-split levels are doubly degenerate [41] so for our case the absorption and emission cross sections are equal.

The values used for $I_{ji}(\nu)$ for the $^2H_{11/2} \rightarrow {}^4I_{15/2}$ were found by fitting the spectra in Figure 4.7 with a sum of Lorentzian distributions of the form Equation 3.1. The center wavelengths for each distribution are taken to be the wavelengths calculated using the energy levels in Table 2.1. The fitting was done using data taken at temperatures that maximized the photoluminescence from these transitions. There was a systematic calibration error that caused a uniform shift of 0.2 nm relative to the calculated wavelength values. The values for h obtained for each peak are used as $I_{ji}(\nu)$ for that transition. A similar approach was taken for the $^4S_{3/2} \rightarrow {}^4I_{15/2}$ transition.

Once the values for $I_{ji}(\nu)$ are extracted, those values along the $Z_1 \rightarrow$ Excited State (for instance E_1) cross sections, σ_{i,Z_1} from Gruber et. al. [51] can be used with Equation 4.20 to calculate the remaining cross sections. Although these are the cross sections for Er^{3+} in Y_2O_3, the crystal field in Y_2O_3 is sufficiently similar to justify their use here [42]. Using the known cross sections simplifies the application of Equation 4.20 because in each case

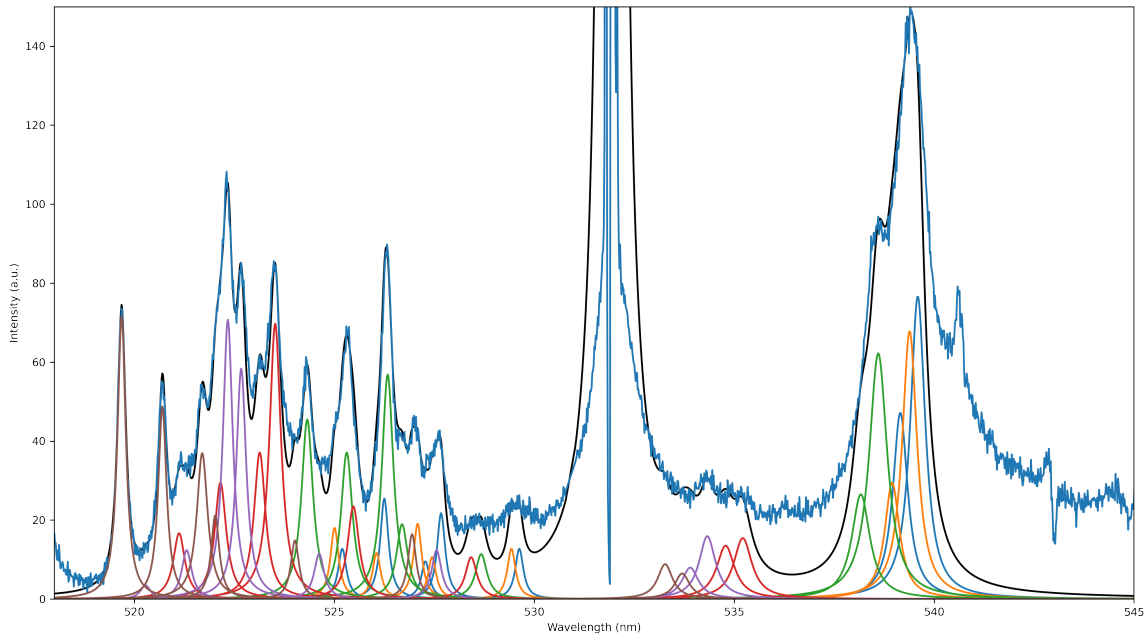

Figure 4.9: Observed $^2H_{11/2} \rightarrow {}^4I_{15/2}$ fit with a sum of Lorentzian distributions.

j=j'so that $\frac{N_j}{N_{j'}} = 1$. The calculated cross sections that will be used in the model are given in Table 4.1.

4.3.5 Phonon Energies and Degeneracies

According to DFT calculations conducted by collaborators [2], there are 48 distinct phonon energies of varying degeneracies, g_p, in Er_2O_3. Table 4.2 gives the theoretical values of the phonon energies along with published values for a majority of the phonon energies. The phonon symmetry symbol identifies both the degeneracy, and the subscript indicates the symmetry upon reflection. For the symmetry symbol A, $g_p = 1$, for E, $g_p = 2$ and for T, $g_p = 3$. For the subscript u means ungerade, the German word for odd, and the subscript g means gerade, the German word for even. Note that any of these phonons can facilitate a transition, assuming the phonon energy is sufficiently close to the energy mismatch between the exciting laser and required transition energy, consistent with the finite bandwidth described above.

Using both experimental observations that show the phonon energies between 4 K and

300 K and the DFT calculations referenced above, the phonon energies of Er_2O_3 shift uniformly to lower energy by around 3-4 cm^{-1} [52; 53; 54]. In the experimental works, much of the observed shift occurred above 80 K. If we look at a well-characterized phonon mode of Lu_2O_3 which is another rare-earth sesquioxide with the same C-type bixbyite crystal structure like Er_2O_3, we see that for that phonon mode, much of the energy shift occurs above 200 K [49]. Turning our attention to the transition energies of Er^{3+} in Er_2O_3. It has been shown that the transition energies between the Stark-split levels of Er^{3+} in Er_2O_3 shift by $\sim$3 cm^{-1} to lower energies. Given that both the phonon energies and the Er^{3+} transition energies shift nearly identically to lower energies as the temperature increases and that most of the shift occurs above 200 K, we will take both quantities as constant between 4 K and 300 K and use the values reported at low temperature ($\sim$10 K). This is also motivated by the fact that not all the phonon modes have experimentally reported values, which means that the theoretical values, which were calculated at 0 K, have to be used. Adopting the experimental values as close to 0 K as possible provides consistency.

The column named 'assumed value' in Table 4.2 is the energy of the phonon mode used in Equations 4.13 and 4.14 to calculate the temperature dependent cross sections. In order to obtain these values, we did the following. First, if there was no experimental measurement of the phonon mode, we took the theoretical value, rounded to the nearest 0.1 cm^{-1}. Those theoretical values are calculated at 0 K. For any mode that has been measured experimentally, we averaged over the low-temperature experimental values, once again rounded to the nearest 0.1 cm^{-1}. Most of the experimental values for the phonon energies have a spread of $\sim$1-2 cm^{-1}, which gives low uncertainty in the phonon energy incorporated into the model. However, there are several modes where the experimental values have a spread of up to 10 cm^{-1}, leading to greater uncertainty. In Chapter 5, we will demonstrate the effect of this greater uncertainty on the output of the model.

4.3.6 Final Form of W_{exc}(T)

There are 64 potential transitions from the 8 ground state Stark levels of the $^4I_{15/2}$ level to the 8 excited state Stark levels of $^2H_{11/2}$ and $^4S_{3/2}$. There are also 48 distinct phonon energies that can facilitate these transitons. Accounting for all possible laser-induced phonon-assisted Stark-Stark excitations between the ground state $^4I_{15/2}$ and the excited states $^2H_{11/2}$ and $^4S_{3/2}$ and all the distinct phonon energies, the final form of W_{exc}(T) is:

$$W_{exc} = \frac{I}{h\nu} N_g \sum_{i=8}^{8} P_{Z_i}(T) \left(\sum_{l=0}^{48} \left(\sum_{j=1}^{6} \sigma_{Z_i,F_j,l}(T) + \sum_{k=1}^{2} \sigma_{Z_i,E_k,l}(T) \right) \right), \tag{4.22}$$

where $\sigma_{Z_i,F_j,l}$(T) and $\sigma_{Z_i,E_k,l}$(T) are the temperature-dependent phonon-assisted excitation cross sections using a phonon of energy ε_l for the $Z_i \rightarrow F_j$ transition and $Z_i \rightarrow E_k$ transition, respectively. The other variables have been defined previously. It is important to note that a majority of the σ_{ijl}(T)≈ 0 because for a majority of possible transitions, $f_{bw,l} \approx 0$. This is because Δ_{ij} is not within the finite energy Lorentzian envelope of the phonon mode with energy ε_l. However, for conciseness and completeness, W_{exc}(T) is written this way. In Chapter 5 the relative contributions of each Stark-Stark transition as a function of temperature will be shown.

4.4 Full Temperature Dependence of N_i(T)

Combining all of expressions above, the temperature dependent population fraction, N_i, is given by:

$$\begin{aligned} N_i(T) = A \sum_{m=8}^{8} P_{Z_m}(T) \left(\sum_{l=0}^{48} \left(\sum_{j=1}^{6} \sigma_{Z_m,F_j,l}(T) + \sum_{k=1}^{2} \sigma_{Z_m,E_k,l}(T) \right) \right) \\ \times P_i(T) \frac{1}{\tau_E \sum_i P_{F_i}(T) + \tau_F \sum_i P_{E_i}(T)}, \end{aligned} \tag{4.23}$$

where A is a constant combining all the temperature independent constants and all other variables have been defined previously. As stated at the start of this chapter, N_i(T) is the

dominant drive of the temperature dependence of the emission from the Er^{3+} ions in the excited state. Therefore, this expression can be normalized and compared to the normalized photoluminescence given in Chapter 3. That will be the focus of Chapter 5.

Table 4.1: The difference (Δ_{ij}) between the transition energy (ε_{ij}) and the laser energy ($h\nu$) at 532.03 nm for all potential Stark-Stark transitions is given. Also given are a majority of the $\sigma_{ij,res}$. Note that we only include cross-sections for 50 $cm^{-1} \leq |\Delta_{ij}| \leq 650$ cm^{-1} because transition with Δ_{ij} outside that range are not expected to contribute to $W_{exc}(T)$ at the experimental laser energy. Transitions with $\Delta_{ij} > 0$ would be anti-Stokes transitions and $\Delta_{ij} < 0$ would be Stokes transitions. Reproduced from [2].

Stark-Stark Transition	$\sigma_{ij,res}$ (1e-20 cm^2)	Δ_{ij} (cm^{-1})
$Z_1 \rightarrow E_1$	0.2	-573.9
$Z_1 \rightarrow E_2$	1.00	-487.9
$Z_1 \rightarrow F_1$	1.40	237.1
$Z_1 \rightarrow F_2$	1.65	244.1
$Z_1 \rightarrow F_3$	1.56	271.1
$Z_1 \rightarrow F_4$	4.55	386.1
$Z_1 \rightarrow F_5$	0.90	417.1
$Z_1 \rightarrow F_6$	5.07	439.1
$Z_2 \rightarrow E_1$	1.34	-611.9
$Z_2 \rightarrow E_2$	1.37	-525.9
$Z_2 \rightarrow F_1$	2.81	199.1
$Z_2 \rightarrow F_2$	1.07	206.1
$Z_2 \rightarrow F_3$	1.28	233.1
$Z_2 \rightarrow F_4$	8.11	348.1
$Z_2 \rightarrow F_5$	3.17	379.1
$Z_2 \rightarrow F_6$	3.48	401.1
$Z_3 \rightarrow E_1$	0.54	-648.9
$Z_3 \rightarrow E_2$	1.38	-562.9
$Z_3 \rightarrow F_1$	1.06	162.1
$Z_3 \rightarrow F_2$	1.77	169.1
$Z_3 \rightarrow F_3$	1.97	196.1

Table 4.1 – continued from previous page

Stark-Stark Transition	$\sigma_{ij,res}$ (1e-20 cm^2)	Δ_{ij} (cm^{-1})
$Z_3 \rightarrow F_4$	10.25	311.1
$Z_3 \rightarrow F_5$	18.20	342.1
$Z_3 \rightarrow F_6$	3.49	364.1
$Z_4 \rightarrow E_1$	-	-661.9
$Z_4 \rightarrow E_2$	2.67	-575.9
$Z_4 \rightarrow F_1$	2.43	149.1
$Z_4 \rightarrow F_2$	0.98	156.1
$Z_4 \rightarrow F_3$	0.66	183.1
$Z_4 \rightarrow F_4$	19.29	298.1
$Z_4 \rightarrow F_5$	15.06	329.1
$Z_4 \rightarrow F_6$	1.52	351.1
$Z_5 \rightarrow E_1$	-	-732.9
$Z_5 \rightarrow E_2$	-	-646.9
$Z_5 \rightarrow F_1$	1.44	78.1
$Z_5 \rightarrow F_2$	1.19	85.1
$Z_5 \rightarrow F_3$	0.40	112.1
$Z_5 \rightarrow F_4$	6.57	227.1
$Z_5 \rightarrow F_5$	3.00	258.1
$Z_5 \rightarrow F_6$	1.08	280.1
$Z_6 \rightarrow E_1$	-	-838.9
$Z_6 \rightarrow E_2$	-	-752.9
$Z_6 \rightarrow F_1$	-	-27.9
$Z_6 \rightarrow F_2$	-	-20.9
$Z_6 \rightarrow F_3$	-	6.1

Table 4.1 – continued from previous page

Stark-Stark Transition	$\sigma_{ij,res}$ (1e-20 cm^2)	Δ_{ij} (cm^{-1})
$Z_6 \rightarrow F_4$	3.01	121.1
$Z_6 \rightarrow F_5$	3.28	152.1
$Z_6 \rightarrow F_6$	1.21	174.1
$Z_7 \rightarrow E_1$	-	-1063.9
$Z_7 \rightarrow E_2$	-	-977.9
$Z_7 \rightarrow F_1$	10.10	-252.9
$Z_7 \rightarrow F_2$	5.25	-245.9
$Z_7 \rightarrow F_3$	1.55	-218.9
$Z_7 \rightarrow F_4$	6.26	-103.9
$Z_7 \rightarrow F_5$	3.65	-72.9
$Z_7 \rightarrow F_6$	1.22	-50.9
$Z_8 \rightarrow E_1$	-	-1078.9
$Z_8 \rightarrow E_2$	-	-992.9
$Z_8 \rightarrow F_1$	16.45	-267.9
$Z_8 \rightarrow F_2$	12.10	-260.9
$Z_8 \rightarrow F_3$	3.64	-233.9
$Z_8 \rightarrow F_4$	7.17	-118.9
$Z_8 \rightarrow F_5$	7.31	-87.9
$Z_8 \rightarrow F_6$	0.89	-65.9

Table 4.2: Calculated phonon frequencies along with their symmetries and degeneracies. We compare our results with previous experimental values and find good agreement. Reproduced from [2].

Symmetry	Frequency (cm^{-1})								
	Present Theory	[55]	[52]	[56]	[53]	[57]	[54]	[58]	Assumed Value
A_u	82.05								82.1
T_u	89.00				90		90		90
E_u	97.33		99.7	99	100	96		99	97.3
T_g	97.62								99.6
T_g	102.34								102.3
T_u	115.03								115
A_g	119.82		123.2		122	120		122	121.8
T_u	126.28		126		128		128		127.3
T_u	133.41		133		135		134		134
T_g	137.01					136		139	139
T_u	146.28				147		146		146.5
E_g	147.15		148	147	145			148	147.5
A_u	174.35								174.4
T_g	177.95								178
E_u	181.89								181.9
T_u	183.25				184		183		183.5
T_g	183.32								183.3
T_u	221.47								221.5
T_u	287.26								287.3
A_u	311.71								311.7
T_u	318.01		316.4						316.4

Table 4.2 – continued from previous page

Symmetry	Frequency (cm^{-1})								
	Present Theory	[55]	[52]	[56]	[53]	[57]	[54]	[58]	Assumed Value
T_g	322.97		323		322	321		322	322.3
T_g	329.51								329.5
T_u	333.24		335		334				334.5
E_g	340.35	336	337.9		338	336		338	338
T_u	357.48								357.5
E_u	358.42								358.4
T_g	360.25				359	359			359
T_u	367.36				375				375
A_g	371.48	374	375	380	381				378
T_g	390.42		391	390		381		381	386
E_u	396.64		395		395				395
E_g	396.94				391	392			391
T_g	405.93	403				404		405	405
T_u	414.56								414.6
A_g	432.19		433.6	434				436	434.8
T_g	442.78	441							441
A_u	451.18								451.2
T_u	466.94		475		476				475
T_g	479.34	479	475	480	485	480		480	479.8
T_u	494.34								494.3
A_u	513.22								513.2
T_g	534.54								534.5

Table 4.2 – continued from previous page

Symmetry	Frequency (cm^{-1})								
	Present Theory	[55]	[52]	[56]	[53]	[57]	[54]	[58]	Assumed Value
T_u	560.38		565		466				565.5
A_g	574.35		576.1						576.1
E_g	580.36					580		580	580
E_u	589.77								589.8
T_g	598.68		598.3	596	600	600		598	598.5

CHAPTER 5

Fitting Observed Temperature Dependent Photoluminesence

In this chapter, we will show the fitting of the model developed in Chapter 4 to the temperature dependent photoluminescence data presented in Chapter 3. We will begin with the fitting procedure and then discuss in turn each parameter; how the parameter affects the model output, what the fit value is, and any conclusion we draw from the values of the fit parameters.

5.1 Fitting Procedure

Embedded in Equation 4.23, there are 4 fitting parameters. They are the lifetimes τ_F and τ_E of the Stark states $^2H_{11/2}$ and $^4S_{3/2}$, respectively, the Pekar-Huang-Rhys constant, S_0, for the Stark-Stark excitations involving $^4S_{3/2}$ and the phonon energy bandwidth Γ. The fitting was conducted only on the photoluminescence observed from the E_1 transitions. As shown in Figures 5.2-5.4, the effect of each parameter is seen in different temperature ranges and only emission from E_1 is observed to have non-zero emission over the entire temperature range. Regardless, it is important to note that the fitting parameters that give good agreement with E_1 give good agreement with the data from the other emission lines.

The fitting is done in the following way. A library of curves is generated over a wide

Parameter	Fit Value
R_{EF}	1111±68
Γ	1.86±0.62 cm^{-1}
S_0 ($^4S_{3/2}$)	0.0045±4e-4

Table 5.1: Fit values and uncertainties due to the uncertainty in the laser wavelength. Units are noted.

range of possible values for the fit parameters. The curves are compared to the observed data from E_1 (shown in Figure 3.4) using a least squares regression. The range of fit parameters is then narrowed around the best fit and the step size for the parameters is reduced. This is repeated until the step size is roughly an order of magnitude smaller than the desired uncertainty. Note that there is additional uncertainty introduced by the measured valued of the laser wavelength (532$\pm$0.03 nm). This is addressed by performing the above procedure between 532 nm and 532.06 nm in steps of 0.01 nm. The resultant parameters and uncertainties are then combined appropriately. The result of these fittings is given in Table 5.1. The model output using the fit values of the parameter are plotted in Figure 5.1.

5.2 Effect of Each Parameter

5.2.1 Stark level lifetimes τ_E and τ_F

Starting with the lifetimes τ_F and τ_E. When we vary these lifetimes, we find that the temperature where the maximum of the normalized temperature dependent photoluminescence occurs for the Stark levels E_1 and E_2 depends only on the ratio $\frac{\tau_E}{\tau_F}$, which we will call R_{EF}. We also observe that the predicted temperature dependent behavior of photoluminescence from the Stark levels of $^2H_{11/2}$, called F_{1-6}, is relatively insensitive, as compared to E_1 and E_2, to the ratio R_{EF}. In addition to R_{EF}, our data also allows us to extract the ratio of the radiative lifetimes:

$$R_{EF,rad} = \frac{\tau_{E,rad}}{\tau_{F,rad}}. \tag{5.1}$$

Using Equation 4.1, we can make a rough estimate of $R_{EF,rad}$. Using the definition $A_i = \frac{1}{\tau_{r,i}}$ we note that the ratio of radiative lifetimes can be rewritten as:

$$R_{EF,rad} = \frac{A_F}{A_E}. \tag{5.2}$$

Using Equations 4.1, 4.4 and 4.5, we see that:

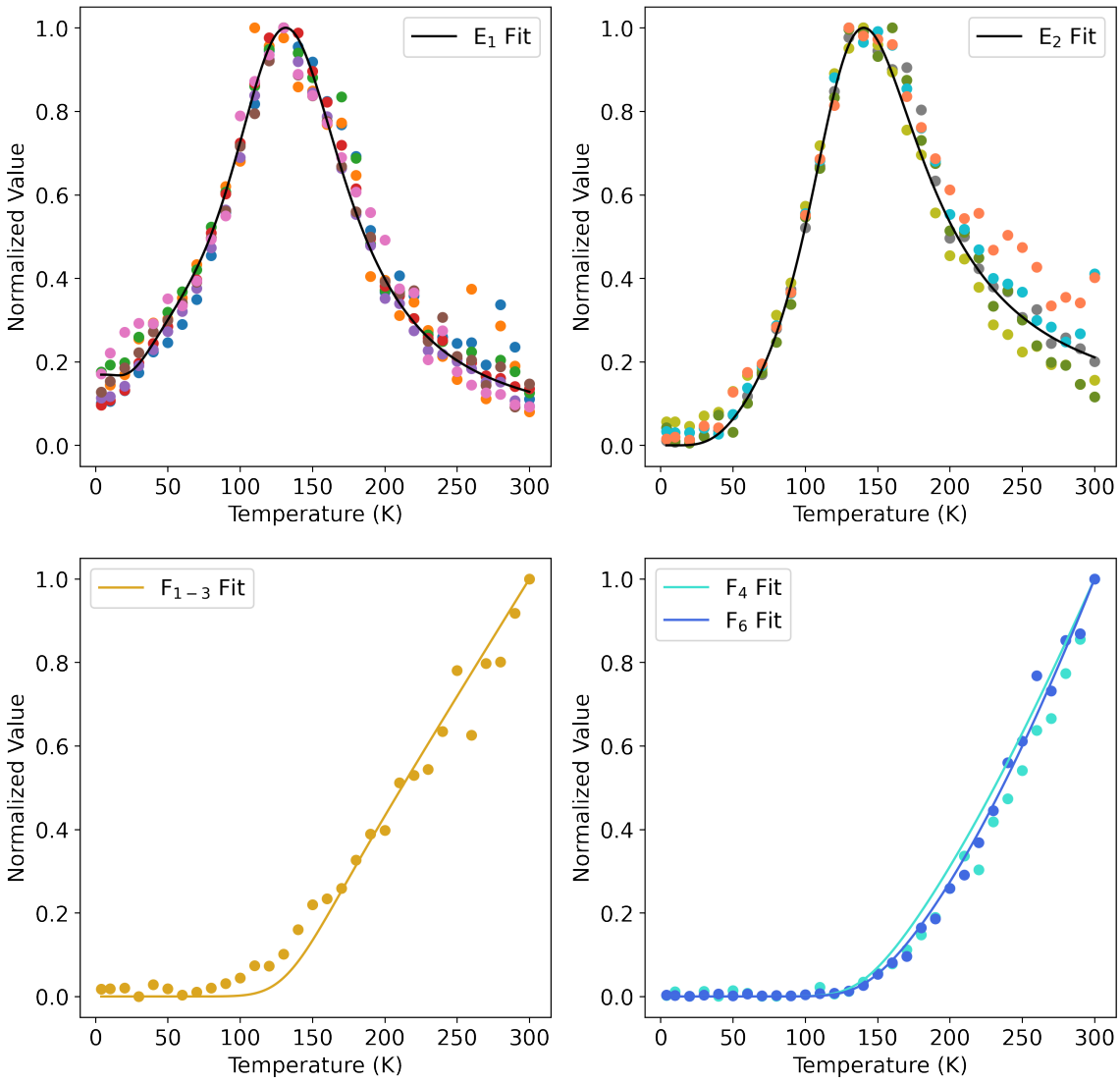

Figure 5.1: Model fits (solid lines) to the normalized measured PL observed (dots) from lines originating from (top left) E_1 and (top right) E_2 of $^4S_{3/2}$ and (bottom left) F_1 and F_2 of $^2H_{11/2}$

$$R_{EF,rad} = \frac{I_F}{I_E}\frac{\sum P_E(T)}{\sum P_F(T)} \tag{5.3}$$

where I_i is the integrated intensity of the respective transition manifold and the summations are over the thermal probabilities given in Equations 4.7 and 4.8. Photoluminescence from the F manifold is readily observed only above 200 K, so this value is calculated between 200 K and 300 K and plotted in Figure 5.1. The average value of $R_{EF,rad}$ is 8.6 and

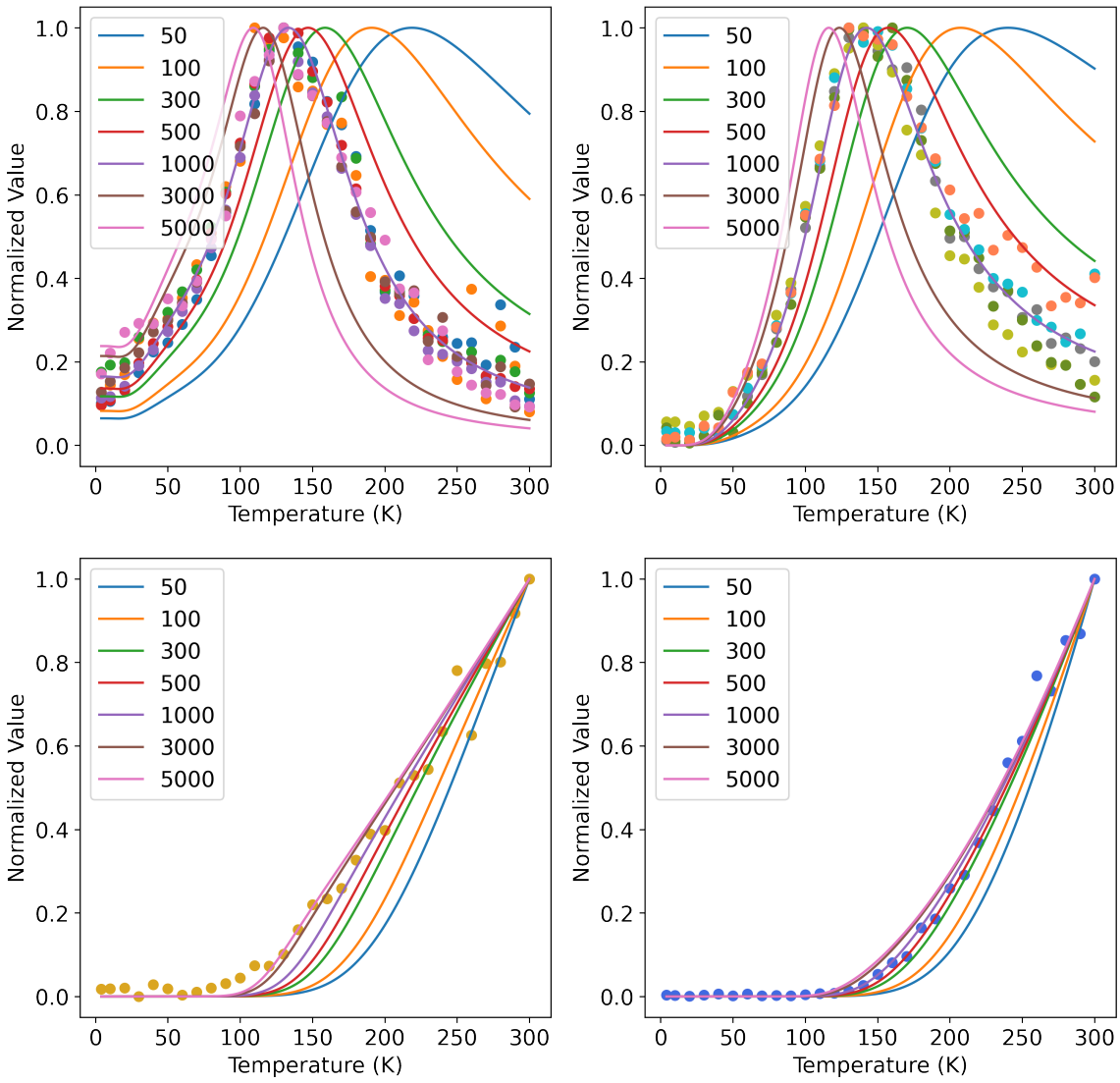

Figure 5.2: Variations in model output as a function of R_{EF} (lines, value noted in the legend) for E_1 (top left), E_2 (top right), $F_{1-3,ave}$ (bottom left) and F_6 (bottom right). The dots are the measured experimental data. The other fit parameters are set to the values reported in Table 5.1

is observed to slowly decrease with increasing temperature.

It is notable that $R_{EF,rad}$ and R_{EF} differ significantly. Given that R_{EF} incorporates both the radiative and non-radiative lifetime, the difference between $R_{EF,rad}$ and R_{EF} demonstrates that Er^{3+} in the F levels decay non-radiatively at a much faster rate than Er^{3+} in the E levels. This is consistent with the finding by M. Dammak et. al. [59] who demonstrated that the $^2H_{11/2}$ levels of Er^{3+} have a stronger electron-lattice coupling that the $^4S_{3/2}$ levels

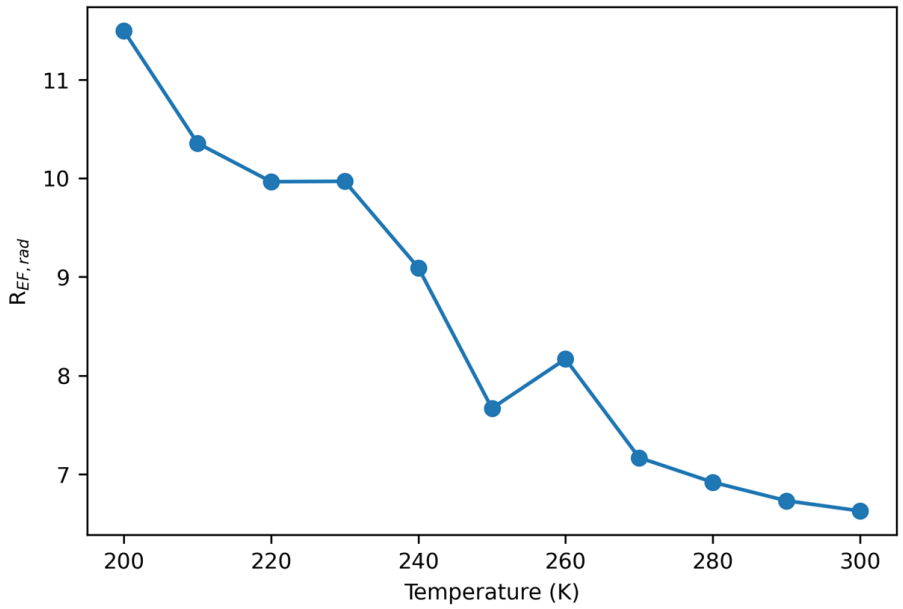

Figure 5.3: $R_{EF,rad}$ between 200 K and 300 K for the $^4S_{3/2} \rightarrow {}^4I_{15/2}$ and $^2H_{11/2} \rightarrow {}^4I_{15/2}$ transition manifolds.

which would lead to an enhanced phonon-assisted decay for Er^{3+} in the $^2H_{11/2}$ levels.

5.2.2 Pekar-Huang-Rhys Constant, S_0

Next is the Pekar-Huang-Rhys constant, S_0. In the previous chapter, we constrained $S_0 \leq 0.01$. As noted above, work by M. Dammak, et. al. [59], showed that the electron-phonon coupling for the $^4S_{3/2}$ state of Er^{3+} is smaller than that of $^2H_{11/2}$. To account for that possibility, a separate S_0 value for excitations involving $^4S_{3/2}$ is introduced as a fitting parameter. In Figure 5.3, we see the effect of varying this value on the model output. The predicted emission from E_1 is affected most strongly, followed by E_2 and the F levels, which show little variation. The main effect is that with increasing S_0, the predicted low temperature photoluminescence from E_1 increases. Further, the temperature where E_1 and E_2 shift to lower temperatures and the overall distribution broadens. The reason for this variation is that all of the phonon-assisted excitation at low temperatures ($<$100 K) involves transitions between $^4I_{15/2}$ and $^4S_{3/2}$ (Figures 5.7 and 5.8). Therefore, changes in the value of S_0 involving those transitions would be most evident at reduced temperatures. The best fit

for this parameter is S_0 =0.0045 and is reported along with the uncertainty in Table 5.1. This value is consistent with the expectation that the electron-phonon coupling to the $^4S_{3/2}$ levels is smaller than the coupling to the $^2H_{11/2}$ levels.

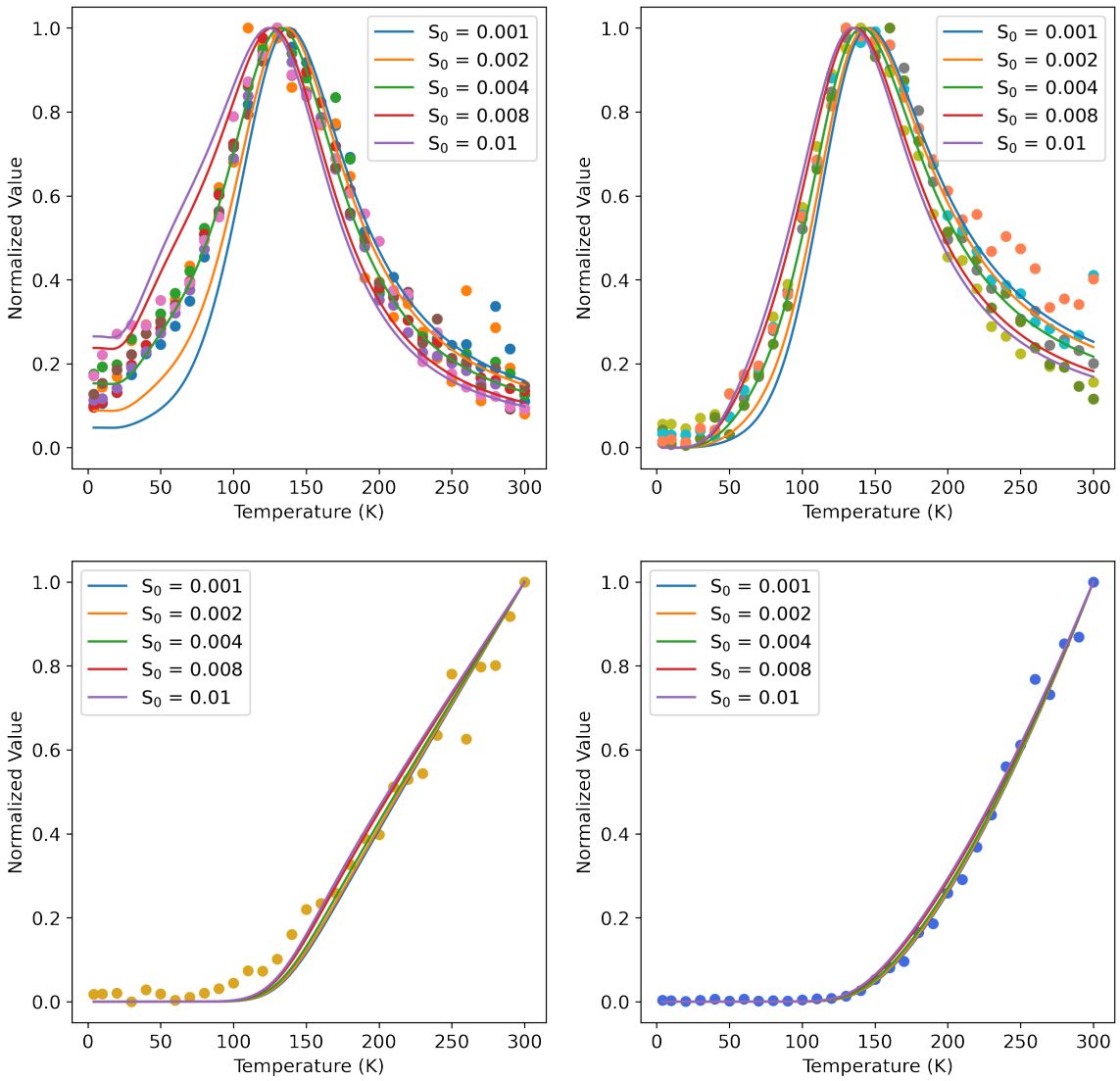

Figure 5.4: Variations in model output as a function of S_0 of the $^4S_{3/2}$ levels for E_1 (top left), E_2 (top right), $F_{1-3,ave}$ (bottom left) and F_6 (bottom right). The other fit parameters are set to the values reported in Table 5.1

5.2.3 Phonon Bandwidth, Γ

Finally, there is the phonon bandwidth Γ. It is important to note that the phonon bandwidth likely varies between phonon modes and varies with temperature. Those complications are

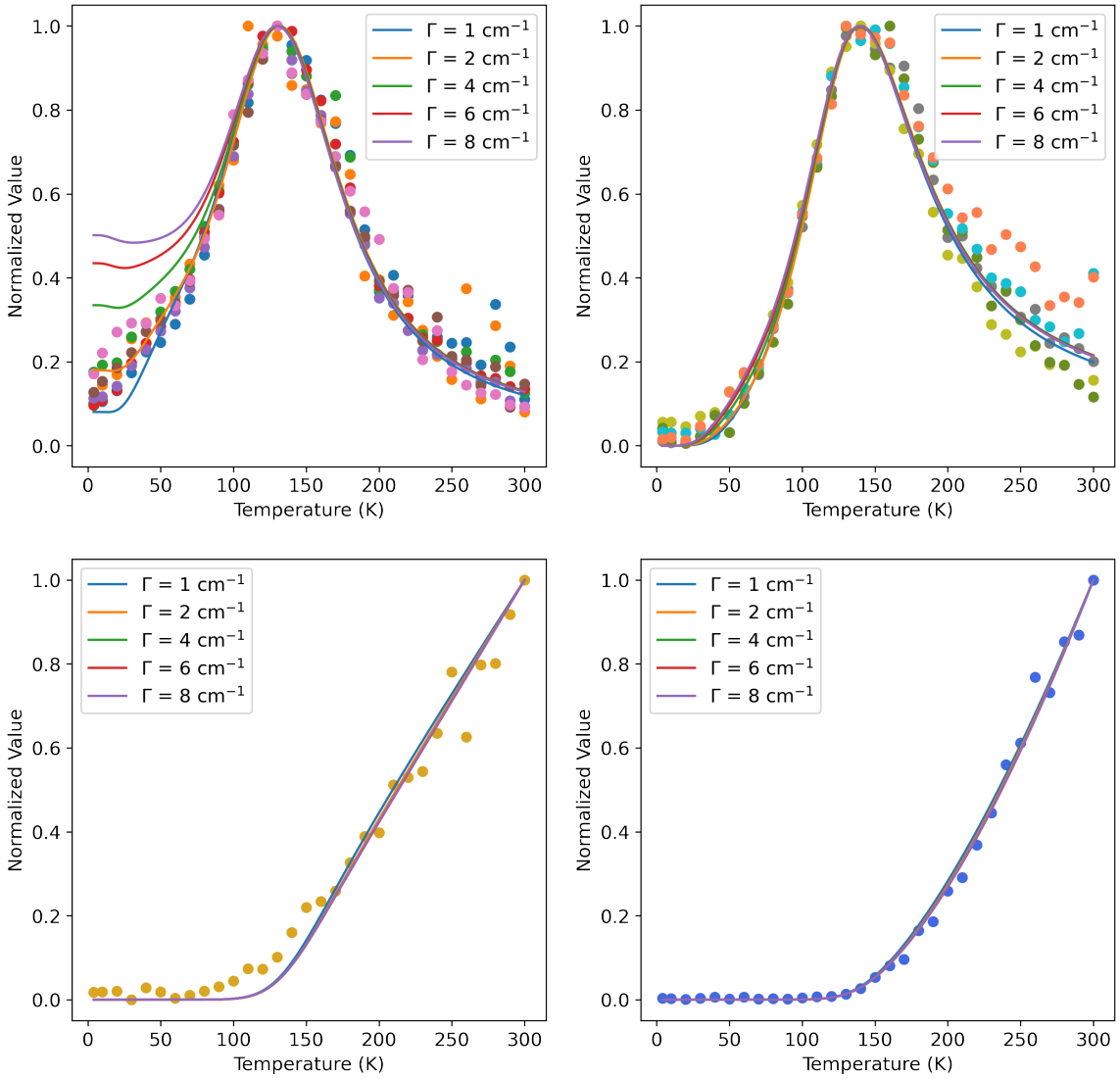

Figure 5.5: Variations in model output as a function of Γ for E_1 (top left), E_2 (top right), $F_{1-3,ave}$ (bottom left) and F_6 (bottom right). The other fit parameters are set to the values reported in Table 5.1

beyond the scope of this thesis and studies to explore them will be suggested in Chapter 6. For the purposes of this thesis, the phonon bandwidth is assumed to be identical for all Er_2O_3 phonon modes and to be constant with temperature. In Figure 5.5, we show the effect of varying Γ on the model output. Note that R_{EF} and S_0 are held constant at the values given in Table 5.1. From this figure it is clear that changing Γ produces appreciable changes in only the predicted emission from the E_1 and that increases in Γ lead to increases in predicted

emission for E_1 below $\sim$75 K. The reason for this variation in the model output is as follows. At reduced temperatures, only a few transitions contribute to the excitation of Er^{3+} and their values of Δ_{ij} are large, relative to the average Δ_{ij} among all potential transitions at higher temperatures. For larger values of Δ_{ij}, increasing Γ raises the contribution of that transition more than for a transition with smaller Δ_{ij}. The average Δ_{ij} among contributing transitions drops with temperature as more transitions participate. Therefore, increasing Γ increases the predicted photoluminescence more at reduced temperature than at elevated temperatures. The best fit for this parameter is 1.86 cm^{-1} and is reported along with the uncertainty in Table 5.1.

5.3 Discussion

5.3.1 Effect of Variation in Phonon Energy

In Chapter 4, it was mentioned that the experimental values for several phonon modes spanned a range of up to 10 cm^{-1}. In order to show the effect of the added uncertainty on the output of the model, we will examine the T_g mode. This mode has a theoretical energy of 390.4 cm^{-1} and the experimental values range between 381 cm^{-1} and 390 cm^{-1}. Using the fit values in Table 5.1, we plot the output of our model as a function of energy of this mode. This is shown in Figure 5.6. It is clear that the model output is relatively insensitive to the uncertainty in this mode. This is because transitions facilitated by this phonon mode are all anti-Stokes at this excitation wavelength. At temperatures where anti-Stokes transitions facilitating this mode become appreciable, the fractional contribution to the overall excitation rate is small. Hence, the model output is insensitive to variations in energy for this mode. If this phonon mode was facilitating Stokes transitions, the effect of the uncertainty would be significant because at reduced temperatures the fractional contribution of Stokes phonon-assisted transitions is large. However, none of the phonon modes which facilitate Stokes transitions have such uncertainty and additional experiments at different exctation wavelengths would be required to interrogate this issue further.

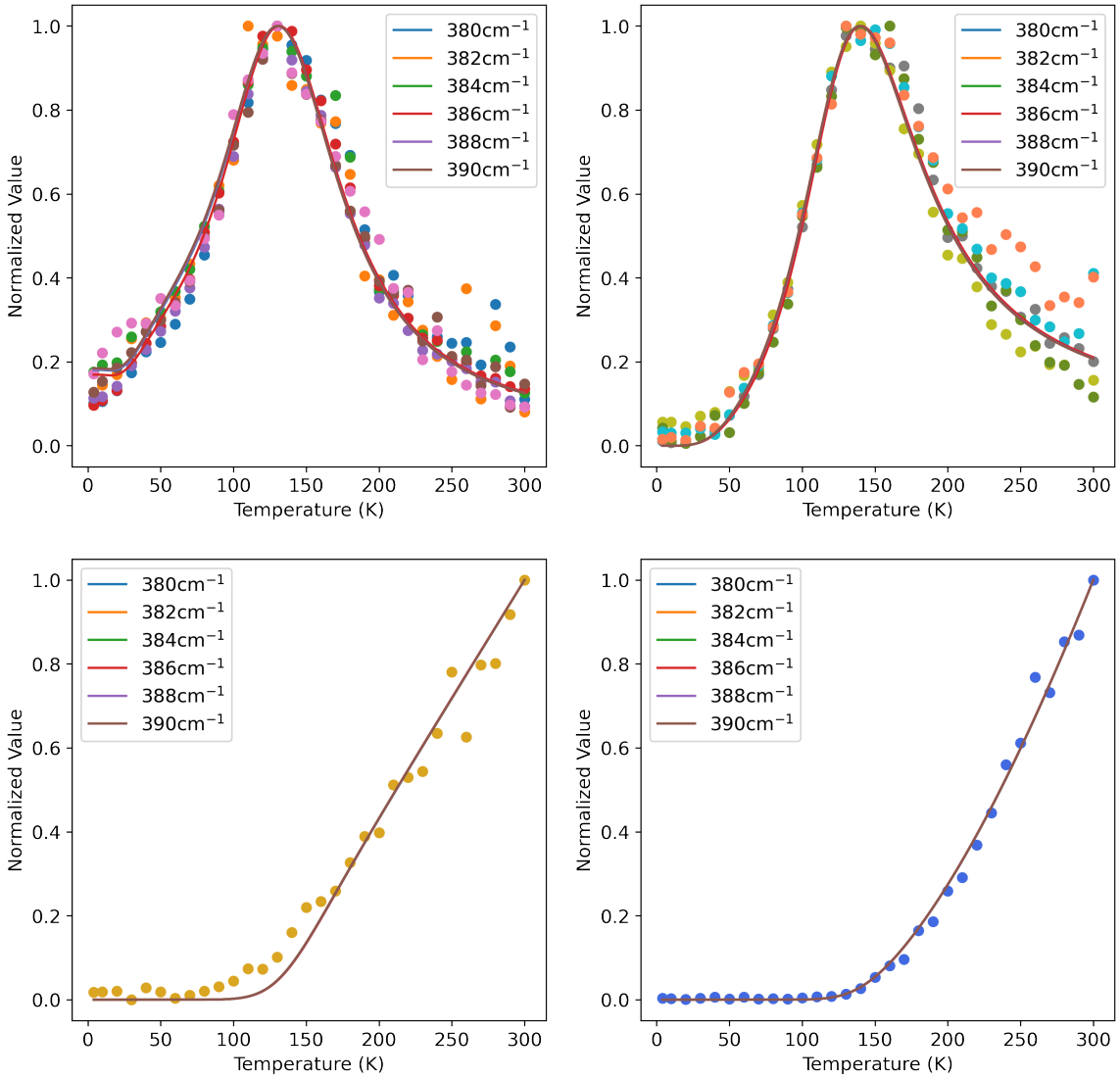

Figure 5.6: Variations in model output as a function of energy of the T_g mode discussed in the text (lines, value noted in the legend). This is shown for E_1 (top left), E_2 (top right), $F_{1-3,ave}$ (bottom left) and F_6 (bottom right). The dots are the measured experimental data.

5.3.2 Contributions of Each Stark-Stark Transition

As noted in Chapter 4, there are 64 transitions between the ground state $^4I_{15/2}$ and the two excited states $^2H_{11/2}$ and $^4S_{3/2}$ that can potentially be facilitated by the 48 distinct energies of the phonon modes in Er_2O_3. Using the fit values in the model, we can show the fractional contribution of each individual Stark-Stark transition as a function of temperature. Following the form of Equation 4.22, for a given Z_i the fraction contribution of a given

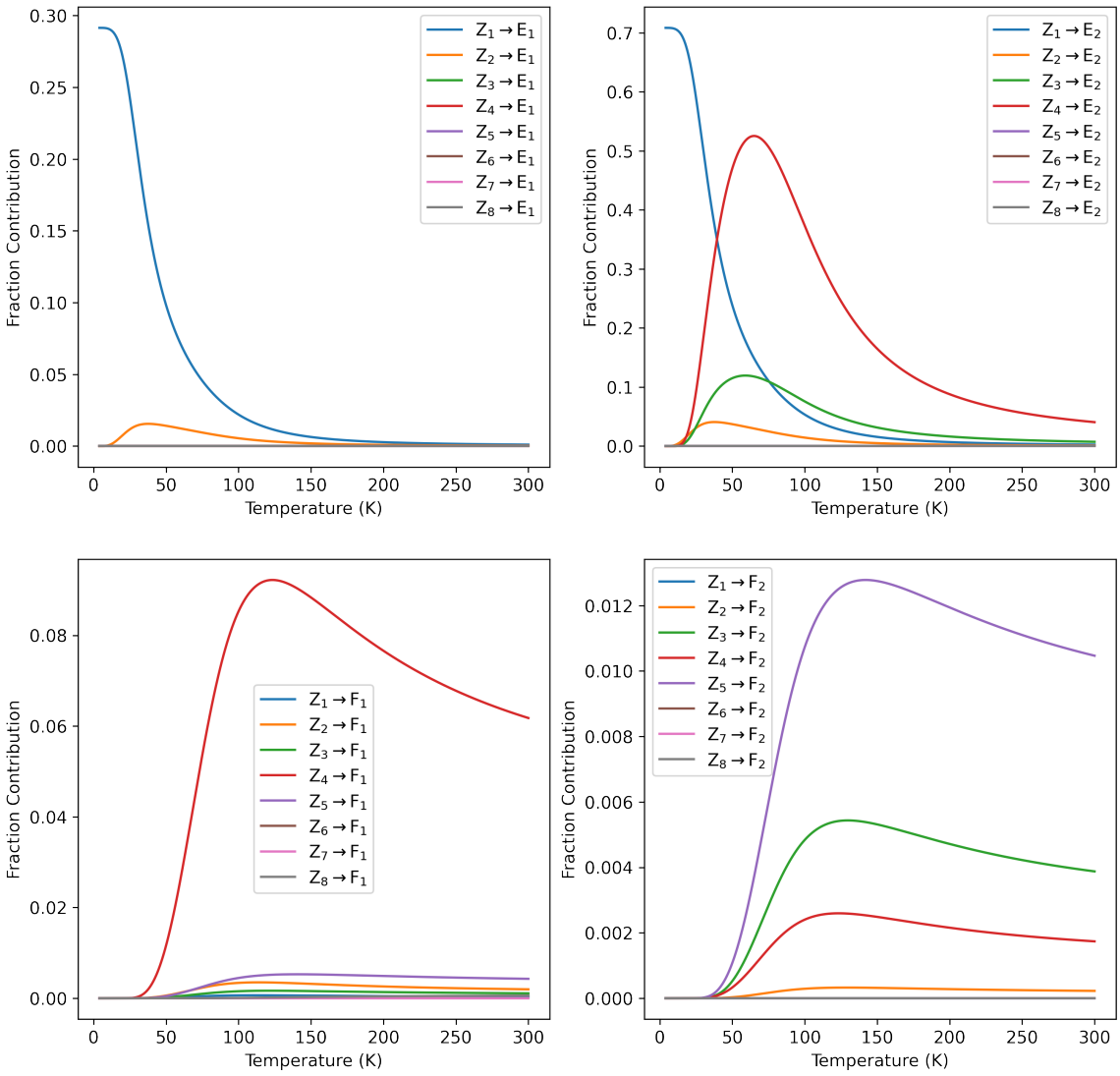

Figure 5.7: Fractional contributions of transitions to E_1 (top left), E_2 (top right), F_1 (bottom left) and F_2 (bottom right) from the ground state Stark levels Z_{1-8} as a function of temperature.

transition is given by:

$$\frac{W_{Z_i,F_j}(T)}{W_{exc}(T)} = \frac{I}{h\nu}\frac{N_g P_{Z_i}(T)\sum_{l=0}^{48}\sigma_{Z_i,F_j,l}(T)}{W_{exc}(T)}, \tag{5.4}$$

$$\frac{W_{Z_i,E_k}(T)}{W_{exc}(T)} = \frac{I}{h\nu}\frac{N_g P_{Z_i}(T)\sum_{l=0}^{48}\sigma_{Z_i,E_k,l}(T)}{W_{exc}(T)}, \tag{5.5}$$

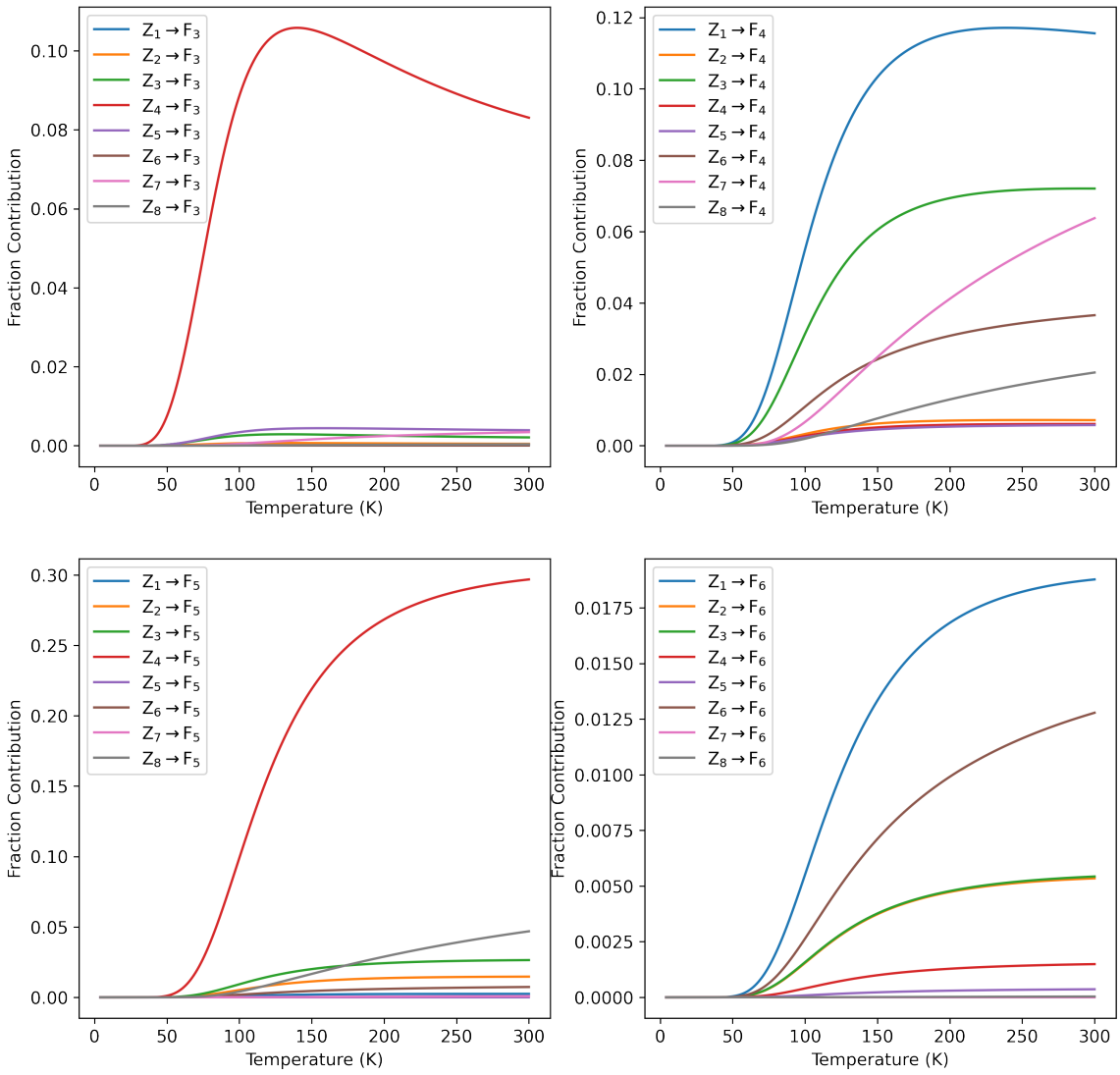

Figure 5.8: Fractional contributions of transitions to F_3 (top left), F_4 (top right), F_5 (bottom left) and F_6 (bottom right) from the ground state Stark levels Z_{1-8} as a function of temperature.

for the Stark levels of $^2H_{11/2}$ and $^4S_{3/2}$, respectively, and $W_{exc}(T)$ is given by Equation 4.22. These fractional contributions are given in Figures 5.7 and 5.8. From this we see that below ~30 K, several transitions dominate and all of the transitions are Stokes transitions. As the temperature is increased, anti-Stokes transitions begin to participate and the number of excitation pathways increases. By 300 K, most of the 64 potential transitions between the Stark levels in the ground state $^4I_{15/2}$ and the excited states $^4S_{3/2}$ and $^2H_{11/2}$ contribute

to the overall excitation rate.

5.3.3 Conceptual Discussion

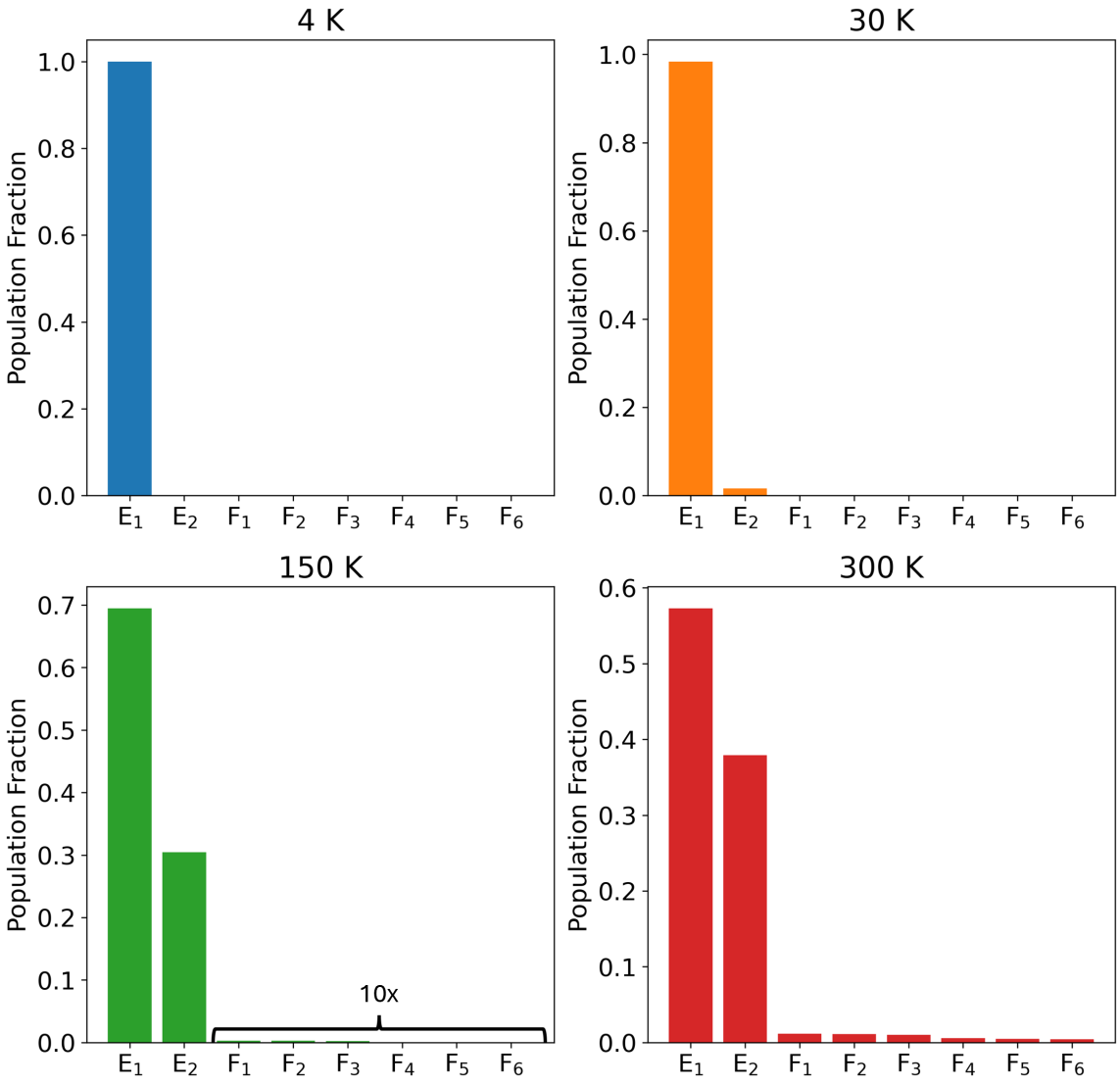

Figure 5.9: Level populations of the Stark-levels of the excited state at several different temperatures. The population fractions at 150 K are multiplied by 10 to show their presence.

We can now give a conceptual understanding of the temperature dependence of the emitted luminescence for a given excited state Stark level. Over the entire temperature range, the Er^{3+} ions in the excited state rapidly thermalize, relative to the excited state lifetime, between all the Stark levels of $^4S_{3/2}$ and $^2H_{11/2}$. This thermalization occurs prior to

any decay to the ground state $^4I_{15/2}$. Therefore, based on Figure 4.2, below the temperature of around 30 K, any Er^{3+} ions in the excited state are only in the E_1 level of the $^4S_{3/2}$ excited state and radiative emission from only this state is observed. As the temperature is raised above 30 K, thermalization causes an appreciable fraction of Er^{3+} ions in the excited state to populate the E_2 level of $^4S_{3/2}$ and radiative emission arising from decays of Er^{3+} in this state is observed. As the temperature is raised above $\sim$150 K, Er^{3+} in the excited state begin to populate the $^2H_{11/2}$ Stark-split levels, called F_{1-6}, and radiative emission begins to be observed from those states as well. The population fraction of all the excited state levels at these temperatures is illustrated in Figure 5.9. This accounts for the onset of emission from each individual Stark-split level.

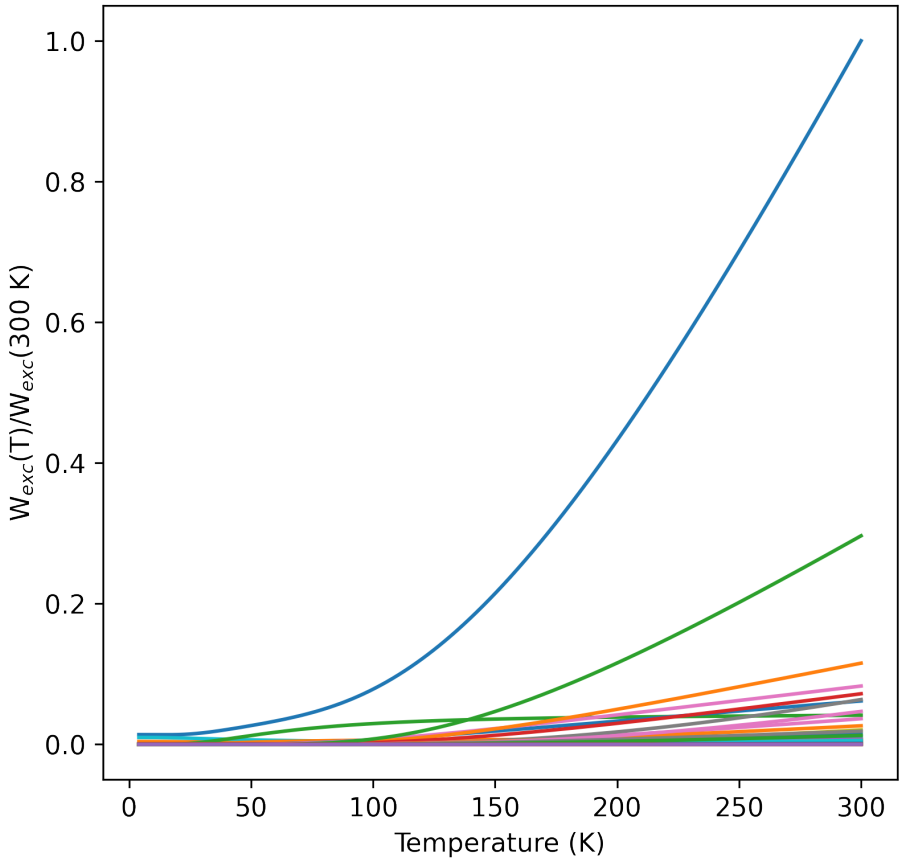

Figure 5.10: $W_{exc}(T)$ (blue) between 4 K and 300 K and normalized to $W_{exc}(300\ K)$. This represents a sum over all 64 transitions (plotted here) out of the ground state $^4I_{15/2}$ that are potentially facilitated by the 48 unique phonon energies of Er_2O_3

All observed increases of photoluminescent emission with increasing temperature results from the monotonic increase of the excitation rate, $W_{exc}(T)$, with temperature as shown in Figure 5.10. This increase is evident at all temperatures for the Stark states of $^2H_{11/2}$ once thermalization begins to populate those levels. However, for the Stark states of $^4S_{3/2}$, this effect is only evident up to around 140 K. This is a direct consequence of the thermalization of states with different intrinsic lifetimes and is described by Equation 4.9. For the present case, the model fit states that the lifetime of Er^{3+} in the $^4S_{3/2}$ levels, called τ_E, is significantly longer than the lifetime of Er^{3+} in the $^2H_{11/2}$ levels, called τ_F. As a result, with increasing temperature, Er^{3+} in the $^4S_{3/2}$ are increasingly emptied via thermal excitation and subsequent decay through the Stark levels of $^2H_{11/2}$. This effect overtakes the monotonic increase of $W_{exc}(T)$ at around 140 K and the emission from $^4S_{3/2}$ begins to decrease with temperature. A pictorial representation of this effect is given in Figure 5.11 for Er^{+3} ions in the E_1 level. The emission is initially weak, increases in strength up to 150 K, then begins to fall because of the competing decay pathways.

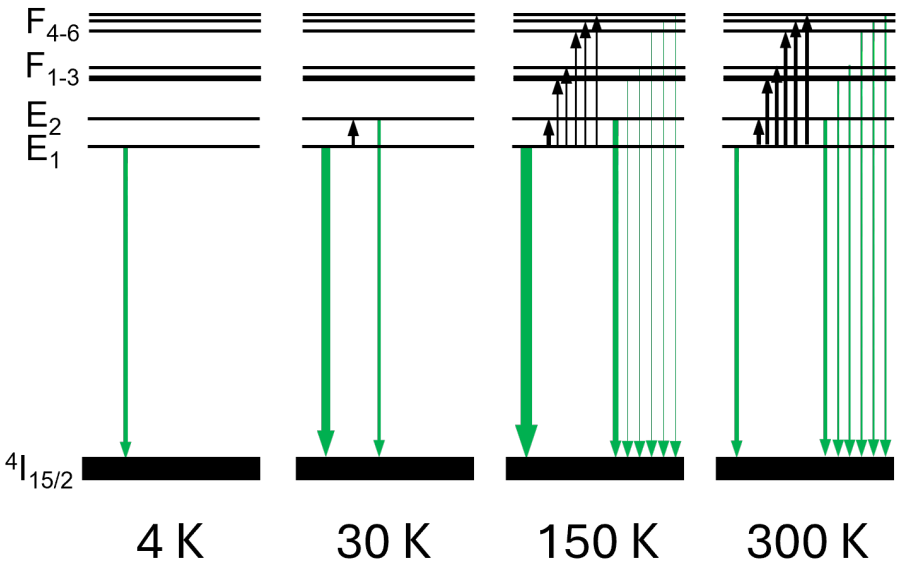

Figure 5.11: Pictorial representation of the decay pathways of Er^{3+} ions in the E_1 state as a function of temperature. The relative strength of emission (green arrows) from each level and thermal excitation to each level (black arrows) is depicted by the thickness of the arrow.

In addition to this conceptual understanding, it is important to note that the observation of non-zero photoluminescence below ∼30 K is a direct consequence of Stokes excitation (Figure 4.6.) If only anti-Stokes excitation is included, which is common for modeled experiments reporting above 150 K [27], the observations cannot be accurately described. This is shown in Figure 5.12, where only a single anti-Stokes transition is incorporated between Z_4 and F_1 using ε_l = 149.1 cm^{-1}, the Er_2O_3 phonon energy closest to Δ_{Z_4,F_1}. This transition is chosen because it is the first anti-Stokes transition to produce non-zero excitation as the temperature is raised from 4 K. Note that R_{EF} is set to 850 to fit the model output to the peaks of E_1 and E_2 and provide a better comparison. The same is true for the case described below.

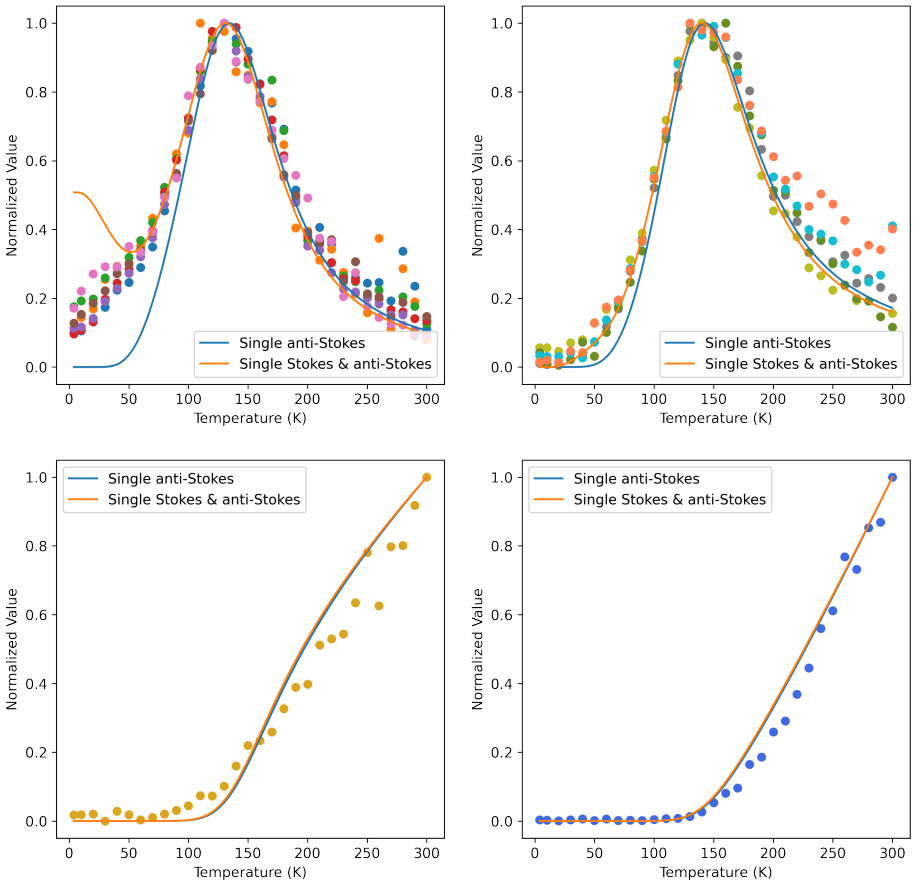

Figure 5.12: Model output for a single anti-Stokes excitation (blue) and for a single anti-Stokes and Stokes excitation (orange) for E_1 (top left), E_2 (top right), $F_{1-3,ave}$ (bottom left) and F_6 (bottom right).

In addition, we find that if Stokes excitations are incorporated, it is necessary to include multiple anti-Stokes excitation pathways to correctly describe our observations above 100 K. Figure 5.12 shows the result of including Z_1 to E_1 transition using ε_l = 576.1 cm^{-1}, the Er_2O_3 phonon energy closest to Δ_{Z_1,E_1}. The Z_4 to F_1 transition used above is also incorporated. The transition Z_1 to E_1 is chosen because it is the weaker of the two excitation pathways that produce non-zero emission at 4 K. In essence, multiple Stokes and anti-Stokes excitation pathways are required to accurately model the observations over the entire temperature range of 4 K to 300 K. This is an important conclusion of this work.

5.3.4 Wavelength Dependence

The model developed in Chapter 4 predicts that under narrowband excitation, such as the laser used in our experiments, the low temperature behavior of photoluminescence from Er^{3+} varies significantly with small shifts ($\sim$0.1 nm) in laser wavelength. Figure 5.6 shows the predicted variation of low temperature photoluminescence over the manufacturing uncertainty of the laser used in the experiments in Chapter 3. While untested, this prediction has important implications for the practical application of optical thermometry systems utilizing two different species of rare earth ions in this temperature range. In fact, recently published paper [8] actually explored this effect for wide bandwidth sources. We are currently working to validate this prediction.

5.4 Conclusion

As a result of fitting the model to the observations in Chapter 3, we are able to draw several important conclusions. First, it is clear that accurate modeling over the measured temperature range requires incorporating multiple Stokes and anti-Stokes phonon assisted transitions. This further requires that we treat the individual Stark-split levels and incorporate the material specific phonons of Er_2O_3 in that model. Second, we are able to conclude that the electron-phonon coupling of Er^{3+} is stronger for the Stark-split levels of $^2H_{11/2}$ as compared to those of $^4S_{3/2}$. Finally, we are able to show a notable prediction of the model

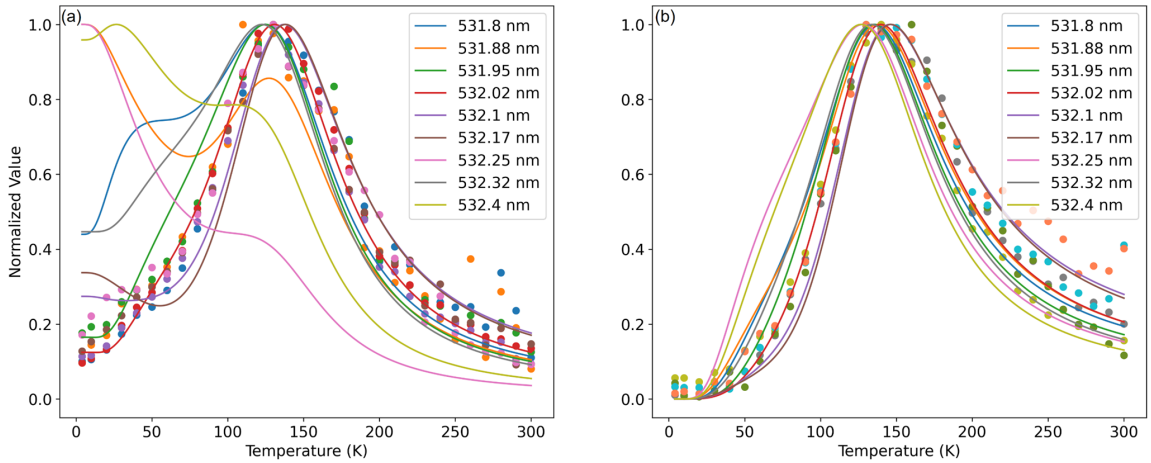

Figure 5.13: Variation in predicted temperature dependence of E_1 (a) and E_2 (b) transitions as a function of excitation wavelength. Note that these are normalized to show the variation in temperature dependent behavior. The predicted absolute values vary by $\sim$10x for E_1 (a) and $\sim$5x for E_2 (b). Dots are measured experimental data. Reproduced from [2].

we developed. Namely, the low temperature photoluminescent behavior of Er^{3+} ions in the Stark levels of $^4S_{3/2}$ varies significantly with small shifts ($\sim$0.1 nm) in excitation wavelength – an untested prediction with important implications in applications such as optical thermometry.

CHAPTER 6

Conclusions and Outlook

In conclusion, we have studied the electron-phonon interactions of Er^{3+} in Er_2O_3 by reporting and modeling new measurements of the temperature dependence of the photoluminescence from the $^4S_{3/2} \rightarrow {}^4I_{15/2}$, $^4S_{3/2} \rightarrow {}^4I_{13/2}$ and $^2H_{11/2} \rightarrow {}^4I_{15/2}$ transition manifolds of Er^{3+} in Er_2O_3. Our modeling approach advanced and improved existing approaches and yielded important insights into the electron-phonon interactions of Er^{3+} with its host lattice.

Specifically, in Chapter 3, we established experimentally that the observed temperature dependence of each individual Stark-Stark transition within each transition manifold was dominated by the temperature dependence of the population fraction of the decaying level, $N_i(T)$. This motivated considering the individual Stark-split levels of the $^{2S+1}L_j$ states. Further, the observation of non-zero photoluminescence below 30 K demonstrated that Stokes excitation is required. Then in Chapter 4, we advanced existing theory to accurately model our observations over the entire temperature range from 4 K to 300 K and in Chapter 5, we fit that model to the data observed in Chapter 3. In doing so, we showed the necessity of the following considerations: First, one needs to consider both Stokes and anti-Stokes excitations rather than a single Stokes or anti-Stokes excitation from the ground state. Omitting either type of transition prevents an accurate description over the measured temperature range. Second, because both Stokes and anti-Stokes excitations must be considered, the individual Stark-split levels in both the excited and ground states must be treated instead of grouping them into their respective manifolds. Finally, because multiple phonon-assisted Stokes and anti-Stokes excitations are required, one must consider the Er_2O_3-specific phonon modes rather than an effective phonon energy for the material.

Besides showing the necessity of the above considerations, we were able to demonstrate

differences in the electron-phonon coupling of the $^2H_{11/2}$ and $^4S_{3/2}$ states. Additionally, we discussed an important untested prediction of the model. Namely, the prediction that the low temperature PL behavior of Er^{3+} in Er_2O_3 varies significantly with small shifts ($\sim$0.1 nm) in excitation wavelength. This possibility has only recently been acknowledged in the literature [8] and it has important implications for rare-earth optical thermometry in this temperature range, especially schemes that utilize multiple ion species. Further, it suggests that one can use wavelength and temperature dependent photoluminescence to probe the interactions between individual Stark levels and specific phonon modes of a material. This is a capability our group is actively pursuing.

6.1 Future Studies

The work described in this thesis suggests the following promising research projects:

(i) As discussed above, the model predicts a significant variation in the low temperature photoluminescence behavior of Er^{3+} photoluminescence as a function of excitation wavelength. Rare-earth optical thermometry is a growing field and understanding the influence of excitation wavelength on expected photoluminescence behavior is vital for system design and implementation. Further validating this model under a variety of excitation conditions would prove useful to that field and provide a technique, namely wavelength and temperature dependent photoluminescence, to study electron-phonon interactions.

(ii) Another direction, alluded to in Chapter 4, is the dependence of Er^{3+} photoluminescence on the thickness of the Er_2O_3 single crystal thin film. Depending on the mechanism for this effect, there are likely significant implications for applications that seek to use nanostructures to enhance rare-earth emission rates including emerging applications in quantum information science.

(iii) Finally, our group has observed a significant enhancement of Er^{3+} photoluminescence after ion irradiation. This effect does not occur for every observed transition

manifold and is contrary to almost all known light emission/solid state systems. It warrants further study given the potential for defect engineering and in light of processing schemes that incorporate Er^{3+} via ion implantation. Both of which have implications for emerging applications of Er^{3+} in quantum information science.

(iv) Our group is uniquely suited to conduct these studies give our use of coherent acoustic phonon (CAP) spectroscopy to study material properties in the near surface region of both damaged and undamaged materials [60; 61; 62; 63; 64].

References

[1] J. B. Gruber, J. Henderson, and M. Muramoto, "Energy Levels of Single-Crystal Erbium," *The Journal of Chemical Physics*, vol. 45, no. 2, pp. 477–482, 1966.

[2] A. Dodson, H. Wu, A. Rai, S. Apte, A. O. Hara, B. Lawrie, Y. Wang, A. Ueda, H. Krzy, M. Titze, J. Davidson, A. Hmelo, A. B. Posadas, A. A. Demkov, S. T. Pantelides, L. C. Feldman, and N. H. Tolk, "Phonon-mediated temperature dependence of Er^{3+} optical transitions in Er_2O_3," *Communications Physics*, vol. 7, no. 69, 2024.

[3] W. C. Martin, R. Zalubas, and L. Hagan, "Atomic Energy Levels - the Rare-Earth Elements.," Tech. Rep. 60, 1978.

[4] B. T. Huy, B. Sengthong, P. V. Do, J. W. Chung, G. A. Kumar, V. X. Quang, V.-d. Dao, and Y.-i. Lee, "A bright yellow light from a Yb3+,Er3+-co-doped Y2SiO5 upconversion luminescence material," *RSC Advances*, vol. 6, no. 95, pp. 92454–92462, 2016.

[5] A. S. Oliveira, E. A. Gouveia, M. T. D. Araujo, and A. S. Gouveia-neto, "Twenty-fold blue upconversion emission enhancement through thermal effects in Pr3+/Yb3+-codoped fluoroindate glasses excited at 1.064 μm," *Journal of Applied Physics*, vol. 87, no. 9, pp. 4274–4278, 2000.

[6] B. Harrington, Z. Ye, L. Signor, and A. D. Pickel, "Luminescence Thermometry Beyond the Biological Realm," *ACS Nanoscience Au*, 2023.

[7] R. Liu, Z. Zhang, Z. Yang, W. Wang, K. Yan, M. Song, and R. Wang, "Erbium-doped Ga2O3 waveguide for optical amplification," *Applied Physics Letters*, vol. 123, no. 15, 2023.

[8] A. De, M. A. Hernández-Rodríguez, A. N. Carneiro Neto, V. Dwij, V. Sathe, L. D. Carlos, and R. Ranjan, "Resonance/off-resonance excitations: implications on the thermal evolution of Eu^{3+} photoluminescence," *Journal of Materials Chemistry C*, vol. 11, no. 18, pp. 6095–6106, 2023.

[9] A. S. Kuznetsov, S. Sadofev, P. Schäfer, S. Kalusniak, and F. Henneberger, "Single crystalline Er_2O_3:sapphire films as potentially high-gain amplifiers at telecommunication wavelength," *Applied Physics Letters*, vol. 105, no. 19, p. 191111, 2014.

[10] C. W. Thiel, T. Bottger, and R. L. Cone, "Rare-earth-doped materials for applications in quantum information storage and signal processing," *Journal of Luminescence*, vol. 131, no. 3, pp. 353–361, 2011.

[11] D. Pak, A. Nandi, M. Titze, E. S. Bielejec, H. Alaeian, and M. Hosseini, "Long-range cooperative resonances in rare-earth ion arrays inside photonic resonators," *Communications Physics*, vol. 5, no. 1, pp. 1–8, 2022.

[12] D. D. Awschalom, R. Hanson, J. Wrachtrup, and B. B. Zhou, "Quantum technologies with optically interfaced solid-state spins," *Nature Photonics*, vol. 12, no. 9, pp. 516–527, 2018.

[13] M. Raha, S. Chen, C. M. Phenicie, S. Ourari, A. M. Dibos, and J. D. Thompson, "Optical quantum nondemolition measurement of a single rare earth ion qubit," *Nature Communications*, no. 2020, pp. 1–6.

[14] B. Judd, "Optical Absorption Intensities of Rare-Earth Ions," *Physical Review*, vol. 127, no. 3, pp. 750–761, 1962.

[15] G. Ofelt, "Intensities of Crystal Spectra of Rare-Earth Ions," *The Journal of Chemical Physics*, vol. 37, no. 3, pp. 511–520, 1962.

[16] B. M. Walsh, *Judd-Ofelt theory: Principles and practices*. 2006.

[17] M. P. Hehlen, M. G. Brik, and K. W. Krämer, "50th anniversary of the Judd-Ofelt theory: An experimentalist's view of the formalism and its application," *Journal of Luminescence*, vol. 136, pp. 221–239, 2013.

[18] F. Auzel, "Multiphonon-assisted anti-Stokes and Stokes fluorescence of triply ionized rare-earth ions," *Physical Review B*, vol. 13, no. 7, pp. 2809–2817, 1976.

[19] F. Auzel, G. F. De Sa', and W. M. de Azevedo, "An example of concentration sensitive electron-phonon coupling in $((C_4H_9)_4N)_3$ $Eu_xY_{1-x}(NCS)_6$ and a new hypothesis for self-quenching," *Journal of Luminescence*, vol. 21, no. 2, pp. 187–192, 1980.

[20] Y. Zhanci, H. Shihua, L. Shaozhe, and C. Baojiu, "Radiative transition quantum efficiency of $^2H_{11/2}$ and $^4S_{3/2}$ states of trivalent erbium ion in oxyfluoride tellurite glass," *Journal of Non-Crystalline Solids*, vol. 343, no. 1-3, pp. 154–158, 2004.

[21] H. Lou, X. Wang, Z. Tao, F. Lu, Z. Jiang, L. Mai, and F. Xu, "Temperature-dependent photoluminescence spectra of Er-Tm-codoped Al_2O_3 thin film," *Applied Surface Science*, vol. 255, no. 19, pp. 8217–8220, 2009.

[22] S. Wang, Y. Ruan, T. Tsuboi, H. Tong, Y. Wang, and S. Zhang, "Temperature dependence of luminescence behavior in Er^{3+}-doped BaY_2F_8 single crystal," *Physica B: Condensed Matter*, vol. 431, pp. 37–43, 2013.

[23] J. A. Capobianco, F. Vetrone, J. C. Boyer, A. Speghini, and M. Bettinelli, "Visible upconversion of Er^{3+} doped nanocrystalline and bulk Lu_2O_3," *Optical Materials*, vol. 19, pp. 259–268, 2002.

[24] C. J. Da Silva and M. T. De Araujo, "Thermal effect on upconversion fluorescence emission in Er^{3+}-doped chalcogenide glasses under anti-stokes, stokes and resonant excitation," *Optical Materials*, vol. 22, no. 3, pp. 275–282, 2003.

[25] N. M. Bhiri, M. Dammak, M. Aguiló, F. Díaz, J. J. Carvajal, and M. C. Pujol, "Stokes and anti-Stokes operating conditions dependent luminescence thermometric performance of Er^{3+}-doped and Er^{3+}, Yb^{3+} co-doped $GdVO_4$ microparticles in the non-saturation regime," *Journal of Alloys and Compounds*, vol. 814, 2020.

[26] C. Koepke, K. Wisniewski, and M. Środa, "Primary- and upconverted emission in the glass and glass-ceramics doped with Er^{3+} ions in the context of maximum phonons," *Journal of Alloys and Compounds*, vol. 883, 2021.

[27] H. Omi, T. Tawara, and M. Tateishi, "Real-time synchrotoron radiation X-ray diffraction and abnormal temperature dependence of photoluminescence from erbium silicates on SiO_2/Si substrates," *AIP Advances*, vol. 2, no. 1, p. 012141, 2012.

[28] P. V. Dos Santos, E. A. Gouveia, M. T. De Araujo, A. S. Gouveia-Neto, A. S. Sombra, and J. A. Medeiros Neto, "Thermally induced threefold upconversion emission enhancement in nonresonant excited Er^{3+}/Yb^{3+}-codoped chalcogenide glass," *Applied Physics Letters*, vol. 74, no. 24, pp. 3607–3609, 1999.

[29] S. Adachi, Y. Kawakami, R. Kaji, T. Tawara, and H. Omi, "Investigation of population dynamics in 1.54-μm telecom transitions of epitaxial $(Er_xSc_{1-x})_2O_3$ thin layers for coherent population manipulation: Weak excitation regime," *Applied Sciences (Switzerland)*, vol. 8, no. 6, pp. 1–13, 2018.

[30] B. Monemar and H. Titze, "Infrared excitation of visible Er^{3+}-luminescence in Yb^{3+}-sensitized YF_3," *Physica Scripta*, vol. 4, no. 1-2, pp. 83–88, 1971.

[31] H. Choi, Y. H. Shin, and Y. Kim, "Temperature Dependence of the Stark Shifts of Er^{3+} Transitions in Er_2O_3 Thin Films on Si(001)," *Journal of the Korean Physical Society*, vol. 76, no. 12, pp. 1092–1095, 2020.

[32] P. Kisliuk, W. Krupke, and J. B. Gruber, "Excited-State Dynamics of Er^{3+} in Gd_2O_3 Nanocrystals," *The Journal of Physical Chemistry C*, vol. 111, no. 27, pp. 9638–9643, 2007.

[33] H. Omi and T. Tawara, "Energy transfers between Er^{3+} ions located at the two crystalographic sites of Er_2O_3 grown on Si(111)," *Japanese Journal of Applied Physics*, vol. 51, no. 2 PART 2, pp. 2–5, 2012.

[34] C. J. Da Silva, M. T. De Araujo, E. A. Gouveia, and A. S. Gouveia-Neto, "Thermal effect on multiphonon-assisted anti-Stokes excited upconversion fluorescence emission in Yb^{3+}-sensitized Er^{3+}-doped optical fiber," *Applied Physics B: Lasers and Optics*, vol. 70, no. 2, pp. 185–188, 2000.

[35] S. Saha, S. Prusty, S. Singh, R. Suryanarayanan, A. Revcolevschi, and A. K. Sood, "Anomalous temperature dependence of phonons and photoluminescence bands in pyrochlore $Er_2Ti_2O_7$: Signatures of structural deformation at 130K," *Journal of Physics Condensed Matter*, vol. 23, no. 44, 2011.

[36] S. A. Goudsmit and P. I. Richards, "the Order of Electron Shells in Ionized Atoms," *Proceedings of the National Academy of Sciences*, vol. 51, no. 4, pp. 664–671, 1964.

[37] T. Engel and P. Reid, *Physical Chemistry*. Pearson Benjamin-Cummings, 2013.

[38] G. L. Miessler, P. J. Fischer, and D. A. Tarr, *Inorganic chemistry*, vol. 27. 1996.

[39] G. Herzberg, *Atomic spectra and atomic structure*. Dover Publications, 1944.

[40] L. Radžiute, D. Kato, G. Gaigalas, P. Jönsson, P. Rynkun, V. Jonauskas, and S. Kučas, "Energy level structure of the ground configuration in the Er3+ free ion," *Physica Scripta*, vol. 90, no. 5, 2015.

[41] H. Kramers, "Théorie générale de la rotation paramagnétique dans les cristaux," *Proceedings of the Royal Netherlands Academy of Ars and Sciences*, vol. 33, pp. 959–972, 1930.

[42] J. B. Gruber, G. W. Burdick, S. Chandra, and D. K. Sardar, "Analyses of the ultraviolet spectra of Er^{3+} in Er_2O_3 and Er^{3+} in Y_2O_3," *Journal of Applied Physics*, vol. 108, no. 2, p. 023109, 2010.

[43] O. Laporte and W. F. Meggers, "SOME RULES OF SPECTRAL STRUCTURE," *Journal of the Optical Society of America*, vol. 12, no. 6, pp. 459–463, 1925.

[44] J. Van Vleck, "The Puzzle of Rare-Earth Spectra in Solids," *Journal of Physical Chemistry*, vol. 41, pp. 67–80, 1936.

[45] D. J. Griffiths and D. F. Schroeter, *Introduction to Quantum Mechanics*. Cambridge University Press, aug 2018.

[46] A. H. Khalid and K. Kontis, "2D surface thermal imaging using rise-time analysis from laser-induced luminescence phosphor thermometry," *Measurement Science and Technology*, vol. 20, p. 025305, feb 2009.

[47] X. Wang, X. Kong, G. Shan, Y. Yu, Y. Sun, L. Feng, K. Chao, S. Lu, and Y. Li, "Luminescence Spectroscopy and Visible Upconversion Properties of Er 3+ in ZnO Nanocrystals," *The Journal of Physical Chemistry B*, vol. 108, pp. 18408–18413, dec 2004.

[48] T. Yokokawa, H. Inokuma, Y. Ohki, H. Nishikawa, and Y. Hama, "Nature of photoluminescence involving transitions from the ground to $4f^{n-1}$ $5d^1$ states in rare-earth-doped glasses," *Journal of Applied Physics*, vol. 77, no. 8, pp. 4013–4017, 1995.

[49] N. Bura, D. Yadav, J. Singh, and N. D. Sharma, "Phonon variations in nano-crystalline lutetium sesquioxide under the influence of varying temperature and pressure," *Journal of Applied Physics*, vol. 126, no. 24, 2019.

[50] B. F. Aull and H. P. Jenssen, "Vibronic Interactions in Nd:YAG Resulting in Nonreciprocity of Absorption and Stimulated Emission Cross Sections," *IEEE Journal of Quantum Electronics*, vol. 18, no. 5, pp. 925–930, 1982.

[51] J. B. Gruber, K. L. Nash, D. K. Sardar, U. V. Valiev, N. Ter-Gabrielyan, and L. D. Merkle, "Modeling optical transitions of Er^{3+} ($4f^{11}$) in C_2 and C_{3i} sites in polycrystalline Y_2O_3," *Journal of Applied Physics*, vol. 104, no. 2, p. 023101, 2008.

[52] G. Schaack and J. A. Koningstein, "Phonon and Electronic Raman Spectra of Cubic Rare-Earth Oxides and Isomorphous Yttrium Oxide*," *Journal of the Optical Society of America*, vol. 60, no. 8, p. 1110, 1970.

[53] J. B. Gruber, R. D. Chirico, and E. F. Westrum Jr., "Correlation of spectral and heat-capacity Schottky contributions for Dy_2O_3 , Er_2O_3 , and Yb_2O_3," *The Journal of Chemical Physics*, vol. 76, no. 9, pp. 4600–4605, 1982.

[54] D. Bloor and J. R. Dean, "Spectroscopy of rare earth oxide systems. I. Far infrared spectra of the rare earth sesquioxides, cerium dioxide and nonstoichiometric praseodymium and terbium oxides," *Journal of Physics C: Solid State Physics*, vol. 5, no. 11, pp. 1237–1252, 1972.

[55] N. Dilawar, S. Mehrotra, D. Varandani, B. V. Kumaraswamy, S. K. Haldar, and A. K. Bandyopadhyay, "A Raman spectroscopic study of C-type rare earth sesquioxides," *Materials Characterization*, vol. 59, no. 4, pp. 462–467, 2008.

[56] J. C. Wang and Y. Y. Zhu, "Study on the structural properties of polycrystalline Er_2O_3 films on Si(001) substrates by Raman spectra," *Advanced Materials Research*, vol. 953-954, pp. 1091–1094, 2014.

[57] D. Yan, P. Wu, S. P. Zhang, L. Liang, F. Yang, Y. L. Pei, and S. Chen, "Assignments of the Raman modes of monoclinic erbium oxide," *Journal of Applied Physics*, vol. 114, no. 19, p. 193502, 2013.

[58] A. M. Lejus and D. Michel, "Raman spectrum of Er_2O_3 sesquioxide," *phys. stat. sol. (b)*, vol. 84, no. 2, pp. K105–K108, 1977.

[59] M. Dammak and D.-l. Zhang, "Spectra and energy levels of Er^{3+} in Er_2O_3 powder," *Journal of Alloys and Compounds*, vol. 407, no. 1-2, pp. 8–15, 2006.

[60] A. Steigerwald, Y. Xu, J. Qi, J. Gregory, X. Liu, J. K. Furdyna, K. Varga, A. B. Hmelo, G. Lüpke, L. C. Feldman, and N. Tolk, "Semiconductor point defect concentration profiles measured using coherent acoustic phonon waves," *Applied Physics Letters*, vol. 94, no. 11, pp. 1–4, 2009.

[61] A. Steigerwald, A. B. Hmelo, K. Varga, L. C. Feldman, and N. Tolk, "Determination of optical damage cross-sections and volumes surrounding ion bombardment tracks in GaAs using coherent acoustic phonon spectroscopy," *Journal of Applied Physics*, vol. 112, no. 1, 2012.

[62] J. Gregory, A. Steigerwald, H. Takahashi, A. Hmelo, and N. Tolk, "Ion implantation induced modification of optical properties in single-crystal diamond studied by coherent acoustic phonon spectroscopy," *Applied Physics Letters*, vol. 101, no. 18, 2012.

[63] A. Baydin, H. Krzyzanowska, M. Dhanunjaya, S. V. Nageswara Rao, J. L. Davidson, L. C. Feldman, and N. H. Tolk, "Depth dependent modification of optical constants arising from H+ implantation in n-type 4H-SiC measured using coherent acoustic phonons," *APL Photonics*, vol. 1, no. 3, 2016.

[64] A. Dodson, A. Baydin, H. Wu, H. Krzyzanowska, and N. Tolk, "Influence of Doping Level on Brillouin Oscillations in GaAs," *Physical Review Applied*, vol. 12, no. 5, pp. 1–10, 2019.